GSSR Waveforms for Lunar Observations

Kevin J. Quirk* and Meera Srinivasan*

ABSTRACT. — To increase the resolution of the Goldstone Solar System Radar (GSSR) for lunar observations, a new ranging waveform must be developed. Several candidate waveforms are identified and analytically characterized, including the existing GSSR biphase-coded (BPC) waveform; two commonly used waveforms, linear frequency modulation (LFM) and Costas frequency-hopped (Costas-FH); and a novel minimum-shift keying (MSK) type waveform developed during the course of this study. A set of requirements taking into consideration the spectrum allocation of the GSSR, the limitations of the transmit power amplifier, and the science objectives for a lunar observation were developed and used as selection criteria for the candidate waveforms. Windowed LFM, windowed Costas-FH, and MSK were identified as suitable for development consideration as a new GSSR ranging waveform for lunar observations.

I. Introduction

The Goldstone Solar System Radar (GSSR) is an instrument within the Deep Space Network (DSN) that is used by scientists to investigate astronomical bodies within the solar system; this includes planets, moons, asteroids, and debris orbiting Earth. Measurements of a body's ephemerides, dynamics, topography, and composition are enabled through the use of radio detection and ranging (radar). Radar works by transmitting a known signal toward an object and measuring the delay, amplitude, Doppler shift, and polarization of any returned echoes. The GSSR is one of two solar system radars on the planet, and it has a number of unique capabilities, including a fully steerable 70-m antenna and real-time signal processing, which enable observations that would either otherwise not be possible or for which the science return would be limited. The GSSR, with its unique capabilities, is crucial to many investigators, both scientific and programmatic. Currently, the primary uses of the instrument are for asteroid investigation for NASA's Science Mission Directorate (SMD), landing site selection for the Human Exploration and Operations Mission Directorate (HEO), and orbital debris investigation for the Office of Safety and Mission Assurance (OSMA).

* Communications Architectures and Research Section.

The research described in this publication was carried out by the Jet Propulsion Laboratory, California Institute of Technology, under a contract with the National Aeronautics and Space Administration.

Currently the GSSR supports two radar waveforms for transmission and processing. The first, continuous waveform (CW), consists of an unmodulated sinusoid that may be hopped between two frequencies to aid in noise reduction. Measurements of amplitude, Doppler shift, and polarization of the returned echoes are processed for the observer. The second waveform is a biphase-coded (BPC) waveform; a pseudonoise (PN) sequence is used to rotate the phase of a sinusoid between two phase offsets 180 deg apart. Measurements of amplitude, Doppler, polarization, and range of the returned echoes are processed for the observer. The BPC waveform, due to its discontinuous phase and large spectral sidelobes, is limited to a main lobe of 16 MHz, providing a maximum range resolution of 18.75 m. Supporting digital elevation maps (DEMs) of the lunar surface with resolutions finer than this will require the introduction of a new radar waveform to the GSSR.

To select the new radar waveform, several candidate waveforms are identified and analytically characterized. To determine their compatibility with GSSR lunar observations, a set of requirements taking into consideration the spectrum allocation of the GSSR, the limitations of the transmit power amplifier, and the science objectives for a lunar observation are formed. Upon applying these requirements to the waveforms, several are identified for development; in the development stage, further characterization of the waveform, including degradation due to implementation impairments, will be undertaken and experimentation performed prior to fielding it as an operational waveform in the GSSR.

We will begin in Section II with a discussion of properties the candidate waveforms should possess and an identification of several candidate waveforms. In Sections III through VI, the candidate waveforms are analyzed. This is followed by Section VII, where we determine the set of requirements that the candidate waveforms must satisfy for GSSR lunar observations. In Section VIII, the set of requirements is used to compare the candidate waveforms, identifying those suitable for development consideration, followed by the conclusion, Section IX.

II. Waveform Properties

To determine candidate waveforms, note that the distortion from the transmit waveform of the returned echoes provides the measurements of delay, Doppler shift, amplitude, and polarization of each echo. The ability to detect these echoes in noise and distinguish replicas that have undergone distortion in both amplitude and time is paramount. The returned echoes will be received in the presence of broadband thermal noise and will have unknown arrival times and Doppler shifts to their spectral components; the time bandwidth product of the waveform is assumed to be a fraction of the speed of light to range rate ratio, allowing the Doppler shifts to be modeled as a uniform shift to each spectral component of the waveform [1, pp. 56–65]. The optimal detection performance for a known waveform in broadband thermal noise is achieved by passing the received signal through a filter matched to the waveform. As the Doppler shift of an echo is unknown, and having a filter matched to each possible Doppler offset is prohibitively complex, the received signal is typically filtered with the nominal, zero-Doppler-shift waveform. The response of the nominal matched filter to a delayed-Doppler-shifted waveform, referred to as the waveform ambiguity function, is necessary in determining the resolution of the range estimate, the intervals

over which the Doppler and range estimates are unambiguous, and the potential for coupling between the range and Doppler estimates of a given waveform.

For an echo, the matched filter output is the correlation of the waveform with that echo. An estimate of the echo's arrival time, and therefore range, is given by the time at which this correlation reaches its maximum. The ability to distinguish between overlapping echoes, the range resolution, is therefore dependent on the autocorrelation properties of the waveform; waveforms with autocorrelation functions having narrow support and consequently wide spectra provide finer resolution. The unambiguous range interval of the range estimates will depend on the periodicity of the autocorrelation function, which is ultimately limited by the duration of the waveform.

The Doppler frequency shift estimates are formed from the echoes of successive waveforms. For a given range, the Doppler shift estimate is formed by sampling the matched filter output at the time corresponding to that range. This is done for a set of consecutive waveforms, forming a sample sequence from which to estimate the spectrum for that range. The set of Doppler frequencies that can be estimated from these samples is limited to the rate at which the waveforms are transmitted, and the resolution is limited by the number of waveform periods used in forming the estimate. A waveform with a shorter duration provides a wider unambiguous frequency interval for the Doppler estimate; however, this is in opposition to the wider unambiguous range interval of the range estimates provided by a longer-duration waveform. Received echoes with Doppler shifts outside the Doppler estimate frequency interval will be aliased into this interval, creating ambiguous estimates; the matched filter response to waveforms with Doppler shifts greater than this would ideally be limited and must be considered.

Considering the detectability of an echo and fidelity of the estimates of range and Doppler of that echo, several criteria for the candidate waveforms are apparent. The detectability of a signal in broadband thermal noise is proportional to its energy, and the ability to distinguish between delayed replicas (echoes) of a waveform is inversely proportional to the waveform's bandwidth; thus, for a fixed transmit power, waveforms with long durations and large bandwidths are desired. In addition, the need for efficient RF amplification and limited out-of-band power requires waveforms with a constant envelope and low spectral sidelobes; various forms of phase and frequency modulation to meet this need are applicable. The ability of a single matched filter output to unambiguously distinguish between delay and Doppler offsets without coupling, providing fine range resolution and Doppler aliasing rejection, is essential. The opposition between the unambiguous range interval, requiring long-duration waveforms, and the unambiguous Doppler interval, requiring short-duration waveforms, favors waveforms that can be easily extended or contracted to match the range Doppler profile of the object to be observed.

The three most common categories of large time-bandwidth-product waveforms for radar are pulse-repetition frequency modulation (FM), BPC, and frequency-hopped spread spectrum (FHSS). Pulse-repetition FM waveforms are characterized by having a duty cycle less than or equal to unity: the waveform is nonzero for a fraction of its duration as an FM waveform [1, pp. 226–286] [2, pp. 168–190] [3, pp. 583–634]. A duty cycle of less than unity reduces the transmitted energy, thereby decreasing the detectability of the returned echoes.

These waveforms often have Doppler-to-range coupling, where the range estimate is biased by the echo's Doppler shift. A BPC waveform is constructed from a PN sequence by switching the waveform to plus or minus one depending on the PN sequence [3, pp. 533–578] [2, pp. 100–164]. The discontinuous phase of the waveform can result in distortion by the transmit power amplifier, due to amplitude modulation to phase modulation (AM-to-PM) conversion, and the large spectral sidelobes, given limits on out-of-band power, can limit the bandwidth and thus resolution of the waveform. To reduce the spectral sidelobes, allowing increased bandwidth and thus finer range resolution, a polyphase code with band limiting [4] or a more spectrally efficient modulation could be employed. An FHSS waveform is generated by transmitting a sequence of frequencies such that each frequency is transmitted once during a period of the waveform [1, pp. 316–324] [2, pp. 74–85]. The sequence order is typically chosen to decouple the range and Doppler estimates [5,6]. We have chosen four candidate waveforms from these categories: linear frequency modulation (LFM), also known as chirp; minimum-shift keying (MSK); m-sequence BPC; and Costas-FHSS. LFM, m-sequence BPC, and Costas frequency-hopped (Costas-FH) are commonly used forms of pulse-repetition FM, BPC, and FHSS, respectively. MSK is a novel form of BPC developed during the course of this study [7].

III. BPC Waveform

The BPC waveform is described, and an analysis of the waveform's autocorrelation, spectrum, and ambiguity functions is performed. A summary of the waveform characteristics in terms of the duration and bandwidth of the waveform is given.

A. Waveform

A BPC waveform is constructed from a PN sequence by switching the waveform to plus or minus one, depending on the PN sequence, every T_c seconds, as shown in Figure 1. The transmitted signal, $x(t)$, is formed by periodically extending the BPC waveform and modulating it onto a radio frequency (RF) carrier with a frequency ω_c. Writing this in terms of the baseband signal, we have

$$z(t) = \Re\left\{ \sum_{k=-\infty}^{\infty} x(t - kMT_c) e^{j\omega_c t} \right\}, \tag{1}$$

where

$$x(t) = \sum_{n=0}^{M-1} c_n p(t - nT_c),$$

$\{c_n\}$ represents the elements of the PN sequence of length M, and $p(t)$ is a rectangular pulse of duration T_c. As the waveform is periodically extended, the use of an m-sequence [8], with its circular properties, for the PN sequence will result in a uniform autocorrelation sidelobe level. The waveform has a discontinuous phase, which, with band limiting, will result in a nonconstant envelope, leading to potential degradation from AM to PM conversion in a transmit power amplifier operating in saturation [9, pp. 203–209].

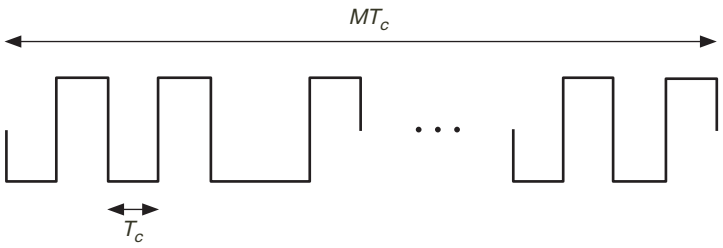

Figure 1. BPC waveform with a chip time T_c and a duration MT_c.

B. Autocorrelation

The autocorrelation function of $z(t)$ is periodic; a single period is given by

$$r(\tau) = \frac{1}{MT_c} \int_{-MT_c/2}^{MT_c/2} z(t)z(t+\tau)\,dt \quad -MT_c/2 \le \tau < MT_c/2$$
$$= \frac{1}{2}\Re\left\{\tilde{r}(\tau)e^{j\omega_c\tau}\right\} \quad -MT_c/2 \le \tau < MT_c/2, \tag{2}$$

where the autocorrelation of the complex baseband signal, $\tilde{r}(\tau)$, assuming the use of an m-sequence [8] for the PN sequence, is determined to be

$$\tilde{r}(\tau) = \begin{cases} 1 - \dfrac{M+1}{M}\dfrac{\tau}{T_c} & |\tau| < T_c \\ -\dfrac{1}{M} & |\tau| \ge T_c. \end{cases}$$

The autocorrelation decays linearly from a peak at $\tau = 0$ to a constant $-1/M$ for delays greater than T_c; the sidelobes are equal to the negative inverse of the code period. The phase of the autocorrelation varies linearly in τ with a slope ω_c. At $\tau = \pm T_c/2$, the autocorrelation is 1/2, and at $\tau = \pm(2-\sqrt{2})T_c/2$, the autocorrelation is $1/\sqrt{2}$. Using the 6 dB and 3 dB extent of the autocorrelation as measures of the delay resolution, we have

$$\Delta_{6\,dB} = T_c$$

and

$$\Delta_{3\,dB} = (2-\sqrt{2})T_c.$$

The magnitude square of the autocorrelation of the complex baseband signal for a BPC waveform with a code period of $M = 2^{17} - 1$ chips is plotted in Figures 2(a) and 2(b). In Figure 2(a), the peak and the adjacent chip times are shown, and in Figure 2(b) the entire unambiguous delay extent is shown. For $|\tau| \ge T_c$, the autocorrelation is –102.35 dB, corresponding to $-1/M$ with $M = 2^{17} - 1$.

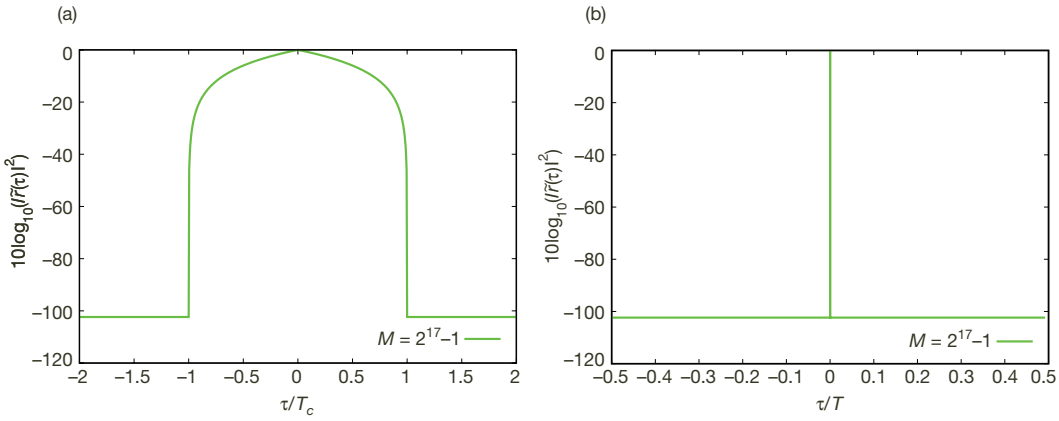

Figure 2. Autocorrelation of the complex baseband BPC signal with $M = 2^{17}-1$ and $T_c = 0.125$ µs: (a) $|\tau| \leq 2T_c$; (b) entire period.

C. Spectrum

To obtain the power spectral density (PSD) of $z(t)$, we first represent the autocorrelation of the complex baseband process in terms of its Fourier Series

$$\tilde{r}(\tau) = \sum_{k=-\infty}^{\infty} a_k e^{jk\frac{2\pi}{MT_c}\tau},$$

where

$$a_k = \begin{cases} \dfrac{1}{M^2} & k = 0 \\ \dfrac{M+1}{M} \dfrac{\sin^2\left(\dfrac{\pi k}{M}\right)}{\left(\dfrac{\pi k}{M}\right)^2} & k \neq 0. \end{cases}$$

Transforming the Fourier Series to a continuous spectrum, we have the PSD of the baseband signal:

$$S_c(\omega) = \frac{2\pi}{M^2}\delta(\omega) + 2\pi\frac{M+1}{M^2} \sum_{\substack{n=-\infty \\ n\neq 0}}^{\infty} \frac{\sin^2\left(\dfrac{\pi n}{M}\right)}{\left(\dfrac{\pi n}{M}\right)^2} \delta\left(\omega - \frac{n2\pi}{MT_c}\right).$$

Using Equation (1), the PSD of the transmitted signal is therefore

$$S(\omega) = \frac{1}{4}S_c(\omega - \omega_c) + \frac{1}{4}S_c^*(-\omega - \omega_c).$$

The spectrum is composed of spectral lines spaced at harmonics of the waveform repetition rate. As the period of the waveform increases, the spacing of the harmonics becomes closer, and their associated power decreases; the total power is constant. The main lobe bandwidth of the waveform is $B = 2/T_c$ Hz.

Figures 3(a) and 3(b) contain plots of the power of the signal in 1-Hz increments for a signal with $T_c = 0.125$ microseconds (μs) and a code length $M = 2^{15} - 1$, as well as for a signal with a code length four times greater, $M = 2^{17} - 1$. In Figure 3(a), the main lobe bandwidths of the two signals are both $2/T_c = 16$ MHz. The spacing of the spectral lines for the shorter code period is 244 Hz, and the longer code period has a spacing four times closer at 61 Hz. The power in the 1-Hz interval containing a spectral line for the longer code period is therefore 6 dB lower, as demonstrated in Figure 3(b), where the line spacing is apparent.

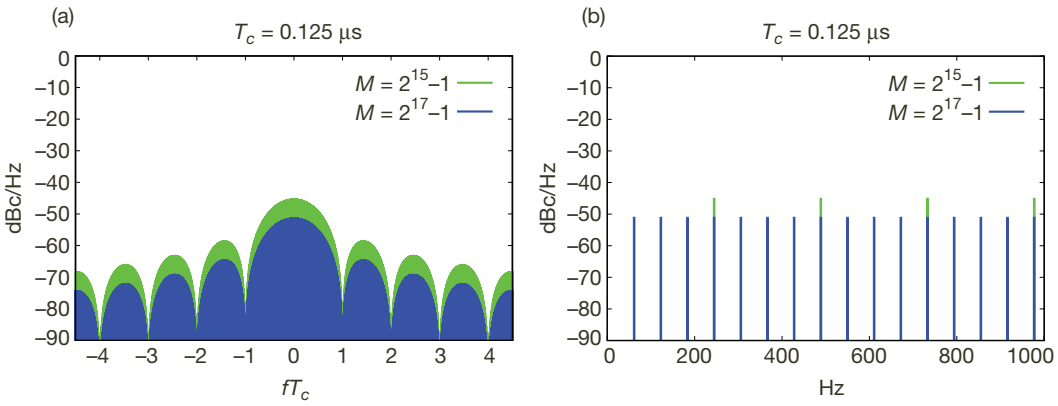

Figure 3. The spectral power in 1-Hz intervals for a pair of BPC waveforms with equal bandwidths, T_c = 0.125 µs, with one having a code period $M = 2^{15}-1$ and the other having a code period $M = 2^{17}-1$: (a) entire spectrum allocation; (b) close up.

D. Ambiguity Function

The ambiguity function of a signal with period T is defined as

$$\xi(\tau, f_d) \triangleq \frac{1}{T} \int_{-T/2}^{T/2} z(t) z(t+\tau) e^{j2\pi f_d t} dt \quad -T/2 \le \tau < T/2.$$

Evaluating this with Equation (1), and defining τ in terms of l integer multiples of T_c and a residual $\hat{\tau}$,

$$l = \left\lfloor \frac{\tau}{T_c} \right\rfloor \quad \hat{\tau} = \tau - lT_c,$$

we have

$$\xi(l, \hat{\tau}, f_d) = \frac{1}{2} \Re\left\{ e^{j\omega_c \tau} \tilde{\xi}(l, \hat{\tau}, f_d) \right\} \quad -T/2 \le \tau < T/2,$$

where

$$\tilde{\xi}(l, \hat{\tau}, f_d) = \frac{e^{-j\pi f_d \hat{\tau}}}{MT_c} \frac{\sin(\pi f_d \hat{\tau})}{\pi f_d} \sum_{n=0}^{M-1} c_n c_{n+1+l} e^{j2\pi f_d (n+1) T_c} + \frac{e^{-j\pi f_d (T_c - \hat{\tau})}}{MT_c} \frac{\sin(\pi f_d (T_c - \hat{\tau}))}{\pi f_d} \sum_{n=0}^{M-1} c_n c_{n+l} e^{j2\pi f_d n T_c}.$$

To determine the domain of Doppler offsets that can be effectively detected, we consider the 1 dB extent of the ambiguity function on the Doppler axis at $\tau = 0$. Setting $\hat{\tau} = 0$ and $l = 0$, the ambiguity function reduces to

$$\tilde{\tilde{\xi}}(0,0,f_d) \approx e^{j\pi f_d T_c(M-2)} \frac{\sin\left(\pi f_d T_c\right)}{\pi f_d T_c} \frac{\sin\left(\pi f_d M T_c\right)}{\pi f_d M T_c}.$$

When $f_d << M/T$, the $sin(x)/x$ response with the first null occurring at $f_d = 1/(MT_c)$ is dominant. Using the 1 dB extent of the main lobe as the effective Doppler domain, Doppler shifts within

$$-\frac{1}{4MT_c} \le f_d \le \frac{1}{4MT_c}$$

are detectable. Relating this to the bandpass signal, the effective Doppler bandwidth is

$$B_{D_{eff}} = \frac{1}{2MT_C}.$$

To find the peak ambiguity function sidelobe, in delay and Doppler, we take the magnitude square of the complex baseband ambiguity function

$$\begin{aligned}
|\tilde{\tilde{\xi}}(l,\hat{\tau},f_d)|^2 = {} & \frac{1}{M^2T_c^2} \frac{\sin^2\left(\pi f_d \hat{\tau}\right)}{\left(\pi f_d\right)^2} \left| \sum_{n=0}^{M-1} c_n c_{n+1+l} e^{j2\pi f_d (n+1) T_c} \right|^2 \\
& + \frac{1}{M^2T_c^2} \frac{\sin^2\left(\pi f_d (T_c - \hat{\tau})\right)}{\left(\pi f_d\right)^2} \left| \sum_{n=0}^{M-1} c_n c_{n+l} e^{j2\pi f_d n T_c} \right|^2 \\
& + \frac{2}{M^2T_c^2} \Re\left\{ \frac{\sin\left(\pi f_d \hat{\tau}\right)\sin\left(\pi f_d (T_c - \hat{\tau})\right)}{\left(\pi f_d\right)^2} \sum_{n=0}^{M-1} \sum_{m=0}^{M-1} c_n c_{n+1+l} c_m c_{m+l} e^{j\left(2\pi f_d T_c\left(n-m+1-\frac{1}{2}\right)\right)} \right\}.
\end{aligned}$$

For the region outside the main lobe, $l \neq \{-1, 0, 1\}$ and $f_d \neq 0$, it can be shown, using Parseval's relation, that

$$\left| \sum_{n=0}^{M-1} c_n c_{n+1+l} e^{j2\pi f_d (n+1) T_c} \right|^2 \approx M + 1.$$

Applying this approximation, we have

$$\begin{aligned}
|\tilde{\tilde{\xi}}(l,\hat{\tau},f_d)|^2 &\approx \frac{(M+1)}{M^2T_c^2} \hat{\tau}^2 \frac{\sin^2\left(\pi f_d \hat{\tau}\right)}{\left(\pi f_d \hat{\tau}\right)^2} + \frac{(M+1)}{M^2T_c^2} \left(T_c - \hat{\tau}\right)^2 \frac{\sin^2\left(\pi f_d (T_c - \hat{\tau})\right)}{\left(\pi f_d (T_c - \hat{\tau})\right)^2} \\
&\quad + \frac{2(M+1)}{M^2T_c^2} \hat{\tau}(T_c - \hat{\tau}) \frac{\sin\left(\pi f_d \hat{\tau}\right)\sin\left(\pi f_d (T_c - \hat{\tau})\right)}{\left(\pi f_d \hat{\tau}\right)\left(\pi f_d (T_c - \hat{\tau})\right)} \\
&\le \frac{(M+1)}{M^2T_c^2} \hat{\tau}^2 + \frac{(M+1)}{M^2T_c^2} \left(T_c - \hat{\tau}\right)^2 + \frac{2(M+1)}{M^2T_c^2} \hat{\tau}(T_c - \hat{\tau}).
\end{aligned}$$

Maximizing this by setting $\hat{\tau} = T_c/2$, the peak ambiguity function sidelobe is given by

$$\tilde{\xi}_{peak} = \frac{1}{\sqrt{M}}.$$

The magnitude square of the ambiguity function of the complex baseband signal is plotted in Figure 4 for a BPC waveform with $T_c = 0.125$ μs and a code period $M = 2^{17} - 1$. In Figure 4, a domain encompassing the main lobe is shown in order to demonstrate the main

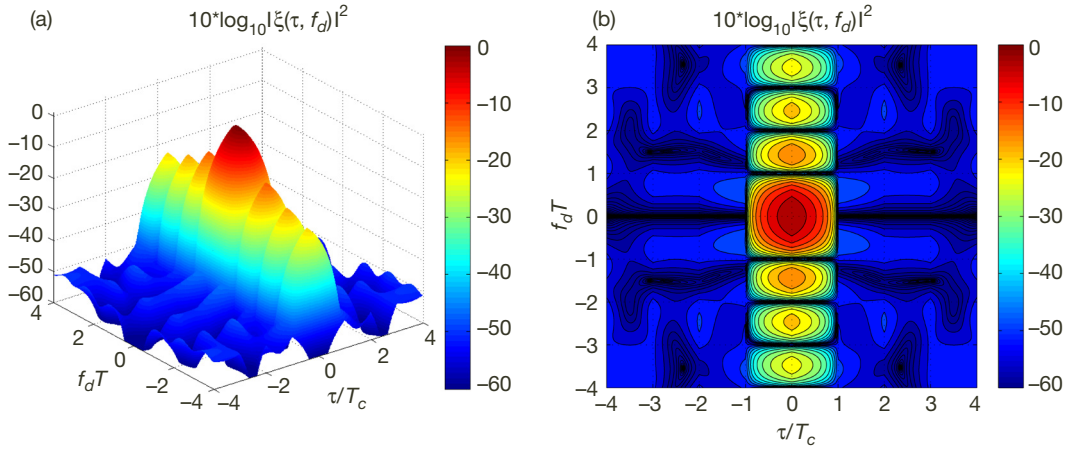

Figure 4. The ambiguity function of the complex baseband BPC waveform, with T_c = 0.125 µs and $M = 2^{17}-1$, encompassing the main lobe: (a) 3-d plot; (b) contour plot.

lobe and peak sidelobe structure of the function. Considering the main lobe, the delay resolution of $\Delta_{6\,dB} = T_c$ is evident along with the effective Doppler resolution of $B_{D_{eff}} = \frac{1}{2T}$. Outside of the main lobe, the peak sidelobes of –51 dB dominate.

E. Waveform Characteristics Summary

For a BPC waveform with a main lobe bandwidth B and a period T, the waveform characteristics are summarized in terms of these parameters (Table 1):

Table 1. Summary of BPSK waveform characteristics.

Phase Switch Rate	$\frac{B}{2}$
Unambiguous Delay Depth	T
Delay Resolution	$\Delta_{3\,dB} = \frac{2(2-\sqrt{2})}{B}$ $\Delta_{6\,dB} = \frac{2}{B}$
Unambiguous Doppler Bandwidth	$\frac{1}{T}$
Effective Doppler Bandwidth	$B_{D_{eff}} = \frac{1}{2T}$
Peak Ambiguity Sidelobe	$\xi_{peak} = \sqrt{\frac{2}{BT}}$

IV. MSK Waveform

The MSK waveform is described, and an analysis of the waveform's autocorrelation, spectrum, and ambiguity functions is performed. A summary of the waveform characteristics in terms of the duration and bandwidth of the waveform is given.

A. Waveform

The transmitted signal, $z(t)$, is formed by periodically extending a waveform that separately modulates the in-phase and quadrature-phase components of the carrier with offset pulse-

shaped PN sequences. To generate this waveform, a pair of periodic PN sequences, $\{c_n^{(i)}\}$ and $\{c_n^{(q)}\}$, are each passed through a pulse-shaping filter with a half sinusoid impulse response, $s(t)$. These shaped PN waveforms are then offset by half a chip time, $T_c/2$, and separately modulated on the in-phase and quadrature phase components of an RF carrier, as shown in Figure 5. Writing the transmitted signal in terms of the baseband signal, we have

$$z(t) = \Re\left\{\sum_{k=-\infty}^{\infty} x(t - kMT_c)e^{j\omega_c t}\right\}, \tag{3}$$

where

$$x(t) = \sum_{n=0}^{M-1} c_n^{(i)} s\left(t - nT_c + \frac{T_c}{2}\right) - j\sum_{m=0}^{M-1} c_m^{(q)} s(t - mT_c),$$

$$s(t) = \begin{cases} \sin\left(\dfrac{\pi t}{T_c}\right) & 0 \le t < T_c \\ 0 & \text{otherwise,} \end{cases}$$

and M is the period of the PN sequences.

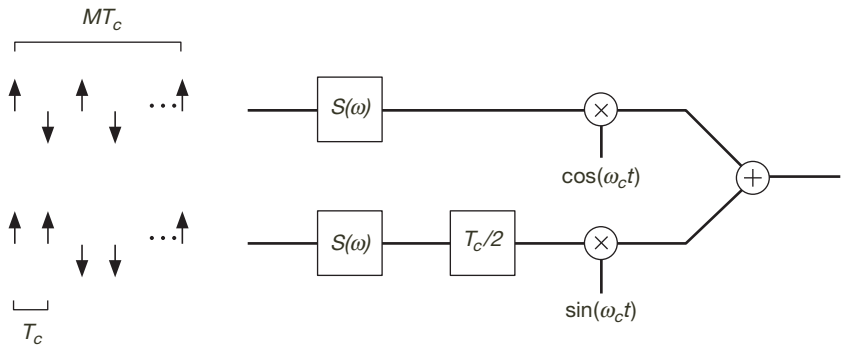

Figure 5. MSK waveform generation, with a chip time T_c and a duration MT_c.

To demonstrate the phase continuity and constant envelope properties of this waveform, the transmitted waveform can equivalently be written as

$$z(t) = d_c(t)\cos\left(\frac{\pi t}{T_c}\right)\cos(\omega_c t) + d_s(t)\sin\left(\frac{\pi t}{T_c}\right)\sin(\omega_c t), \tag{4}$$

where

$$d_c(t) = \sum_{k=-\infty}^{\infty}\sum_{n=0}^{M-1} (-1)^n c_n^{(i)} p\left(t - nT_c + \frac{T_c}{2} - kMT_c\right)$$

and

$$d_s(t) = \sum_{k=-\infty}^{\infty}\sum_{n=0}^{M-1} (-1)^n c_n^{(q)} p(t - nT_c - kMT_c),$$

with $p(t)$ representing a rectangular pulse of duration T_c. Expressing Equation (4) in a magnitude phase form and applying trigonometric identities and properties, we have

$$z(t) = \cos\left(\omega_c t - d_c(t)d_s(t)\frac{\pi t}{T_c} + \phi(t)\right), \tag{5}$$

where

$$\phi(t) = \begin{cases} 0 & d_c(t) = 1 \\ 1 & d_c(t) = -1. \end{cases}$$

Note the waveform has a constant envelope and that the phase continuity can be demonstrated by considering the phase transition at times equal to integer multiples of $T_c/2$. For phase continuity, at the transition $t = kT_c/2$ we require

$$-d_c(kT_c/2)d_s(kT_c/2)\frac{\pi k}{2} + \phi(kT_c/2) = -d_c((k-1)T_c/2)d_s((k-1)T_c/2)\frac{\pi k}{2} + \phi((k-1)T_c/2). \tag{6}$$

When k is odd, the data in the quadrature channel is unchanged; we must therefore satisfy

$$\left(d_c(kT_c/2) - d_c((k-1)T_c/2)\right)\frac{\pi k}{2} = \phi(kT_c/2) - \phi((k-1)T_c/2),$$

which reduces to 0 = 0 when $d_c(kT_c/2) = d_c((k-1)T_c/2$ and $\pm k\pi = \pm\pi$ otherwise. As the arguments to the trigonometric function are modulo 2π, any odd multiple of π is equivalent to π and the expression is true:

$$\left(\pm k\pi\right) \bmod 2\pi = \pm\pi \quad \text{k is odd.}$$

When k is even, Equation (6) becomes

$$\left(d_s(kT_c/2) - d_s((k-1)T_c/2)\right)\frac{\pi k}{2} = 0,$$

which reduces to 0 = 0 when $d_s(kT_c/2) = d_s((k-1)T_c/2)$ and $\pm k\pi = 0$ otherwise. As the arguments to trigonometric function are modulo 2π, an even multiple of π is equivalent to 0 and the expression is true:

$$\left(\pm k\pi\right) \bmod 2\pi = 0.$$

The waveform therefore has a continuous phase that varies linearly $\pm\frac{\pi}{2}$ rad each $T_c/2$ interval. Using Equation (5), we also note that the frequency of the waveform changes by $\pm\frac{\pi}{T_c}$ every $T_c/2$ and can thus be viewed as an MSK-type waveform.

B. Autocorrelation

The autocorrelation function of $z(t)$ is periodic; a single period is given by

$$r(\tau) = \frac{1}{MT_c}\int_{-MT_c/2}^{MT_c/2} z(t)z(t+\tau)\,dt \quad -MT_c/2 \le |\tau| < MT_c/2$$
$$= \frac{1}{2}\Re\{\tilde{r}(\tau)e^{j\omega_c\tau}\},$$

where $\tilde{r}(\tau)$ is the autocorrelation of the complex baseband signal. Defining τ in terms of l integer multiples of T_c and a residual $\hat{\tau}$,

$$l = \left\lfloor \frac{\tau}{T_c} \right\rfloor \quad \hat{\tau} = \tau - lT_c,$$

we have

$$\tilde{r}(l,\hat{\tau}) = \begin{cases} \frac{\alpha_l}{M}\rho(T_c-\hat{\tau}) + \frac{\alpha_{l+1}}{M}\rho(\hat{\tau}) + \frac{j}{2M}\left[(\beta_{l-1}-\beta_{-l})\rho\left(\frac{T_c}{2}-\hat{\tau}\right) + (\beta_l-\beta_{-l-1})\rho\left(\frac{T_c}{2}+\hat{\tau}\right)\right] & 0 \le \hat{\tau} < \frac{T_c}{2} \\ & l \in [-\frac{M}{2},\frac{M}{2}) \\ \frac{\alpha_l}{M}\rho(T_c-\hat{\tau}) + \frac{\alpha_{l+1}}{M}\rho(\hat{\tau}) + \frac{j}{2M}\left[(\beta_l-\beta_{-l-1})\rho\left(\frac{3T_c}{2}-\hat{\tau}\right) + (\beta_{l+1}-\beta_{-l-2})\rho\left(\hat{\tau}-\frac{T_c}{2}\right)\right] & \frac{T_c}{2} \le \hat{\tau} < T_c \\ & l \in [-\frac{M}{2},\frac{M}{2}), \end{cases} \tag{7}$$

where

$$\rho(\tau) \triangleq -\cos\left(\frac{\pi\tau}{T_c}\right)\frac{\tau}{T_c} + \frac{1}{\pi}\sin\left(\frac{\pi\tau}{T_c}\right),$$

$$\alpha_k \triangleq \sum_{n=0}^{M-1} c_n^{(i)} c_{n+k}^{(i)},$$

and

$$\beta_k \triangleq \sum_{n=0}^{M-1} c_n^{(i)} c_{n+k}^{(q)};$$

the autocorrelation functions of the in-phase and quadrature-phase sequences are assumed to be identical, $\alpha_k^{(i)} = \alpha_k^{(q)}$, and the cross-correlation between the in-phase and quadrature-phase sequences satisfies $\beta_k^{(i,q)} = \beta_{-k}^{(q,i)}$.

The autocorrelation has a main lobe, extending from $[-T_c, T_c]$, dominated by

$$\tilde{r}(l,\hat{\tau}) \approx -\cos\left(\frac{\pi}{T_c}(T_c - |\hat{\tau}|)\right)\frac{T_c - |\hat{\tau}|}{T_c} + \frac{1}{\pi}\sin\left(\frac{\pi}{T_c}(T_c - |\hat{\tau}|)\right) \quad l = -1, 0 \;\; |\hat{\tau}| \le T_c.$$

This function has a peak value at $\hat{\tau} = 0$, is zero at $\hat{\tau} = \pm T_c$, and has a cosine response near $\hat{\tau} = 0$, giving way to a more rapid decay as $|\hat{\tau}|$ increases. The autocorrelation is equal to $1/2$ at $\tau = \pm 0.4T_c$ and $1/\sqrt{2}$ at $\tau = \pm 0.28T_c$; the delay resolutions, given as the 6 dB and 3 dB extents of the main lobe of the autocorrelation, are therefore

$$\Delta_{6\,dB} = 0.8T_c$$

and

$$\Delta_{3\,dB} = 0.56T_c.$$

The magnitude square of the autocorrelation function of the complex baseband signal, $\tilde{r}(\tau)$, for delays less than $\pm T_c$ is plotted in Figure 6. Note that the slow roll-off near $\tau = 0$ gives way to a rapid decay, reaching the 6 dB level at $\tau = \pm 0.4T_c$. The autocorrelation of a BPC waveform with an equal chip time, T_c, is also shown. Comparing the two waveforms, the autocorrelation of the MSK waveform exceeds that of the BPC for small τ and drops off more rapidly beyond the delay resolution.

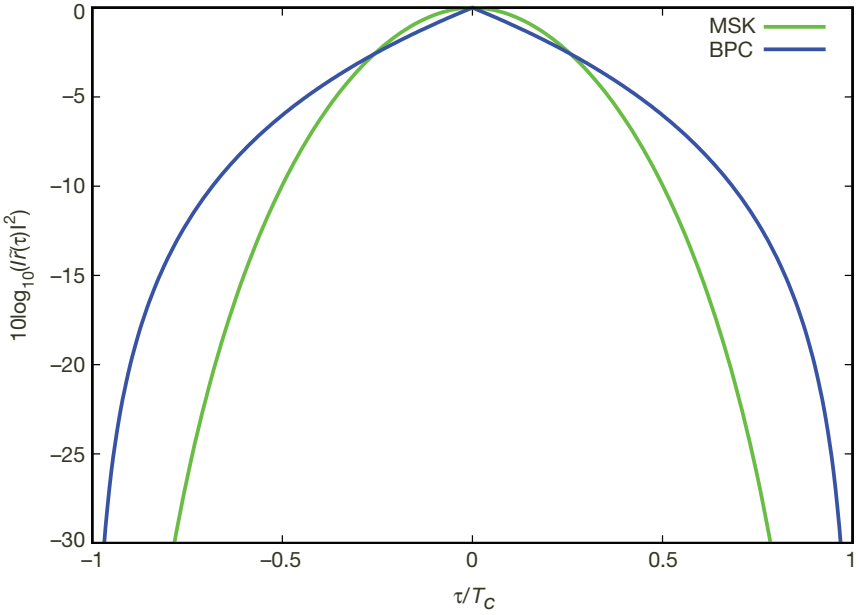

Figure 6. Autocorrelation of a complex baseband MSK waveform and a complex baseband BPC waveform for $|\tau| < 2T_c$.

The peak sidelobe levels of the autocorrelation, Equation (7), are dependent on both the autocorrelations and cross-correlation of the PN sequences; the proper choice of these sequences is vital. One option is to use a preferred pair of m-sequences [8]. An m-sequence has a period $M = 2^n - 1$ for some integer n, and a two-valued autocorrelation,

$$\alpha_k = \begin{cases} M & k = 0 \\ -1 & k \neq 0. \end{cases}$$

A set of preferred pair of m-sequences can be found having a three-valued cross-correlation given by

$$\beta_k = \begin{cases} -1 + 2^{\left\lfloor \frac{n+e}{2} \right\rfloor} & \text{occurs } 2^{n-e-1} + 2^{\frac{n-e-2}{2}} \text{ times} \\ -1 & \text{occurs } 2^n - 2^{n-e} - 1 \text{ times} \\ -1 - 2^{\left\lfloor \frac{n+e}{2} \right\rfloor} & \text{occurs } 2^{n-e-1} - 2^{\frac{n-e-2}{2}} \text{ times,} \end{cases}$$

where we restrict $e = 1$ for odd n and $e = 2$ for even n [8]. In the region outside the main lobe, $|\tau| > T_c$, the cross-correlation terms will dominate, with local maximum values occurring at odd multiples of half the chip time:

$$\tau = \frac{(2m+1)T_c}{2} \quad m = \pm 1, \pm 2, \pm 3 \cdots.$$

To find the peak sidelobe value of the autocorrelation, we evaluate Equation (7) at these delays, giving

$$\tilde{r}\left(l, \frac{T_c}{2}\right) \approx \frac{j}{2M}(\beta_{l+1} - \beta_{-l-2}) \quad l \in \left\{-\frac{M}{2}, \cdots, -2, 1, 2, \cdots \frac{M}{2} - 1\right\}. \tag{8}$$

The cross-correlation difference term can take on one of five possible values

$$(\beta_{l+1} - \beta_{-l-2}) = \begin{cases} 0 \\ \pm 2^{\frac{e}{2}} \sqrt{M+1} \\ \pm 2^{1+\frac{e}{2}} \sqrt{M+1}. \end{cases}$$

Using the cross-correlation that maximizes Equation (8), we have

$$|\tilde{r}(\tau)| \leq \frac{2^{\frac{e}{2}} \sqrt{M+1}}{M} \quad |\tau| \geq T_c.$$

Consider a waveform formed using sequences of length $M = 2^{18} - 1$ with the preferred pair of m-sequences represented by the linear-feedback shift registers $0x404A1$ and $0x40081$. The magnitude square of the autocorrelation function of the complex baseband signal, $\tilde{r}(\tau)$, is shown in Figure 7. The sidelobe structure shows peaks at odd multiples of $T_c/2$ with values –54 dB and –48 dB, corresponding to $\pm\frac{2^{\frac{e}{2}-1}\sqrt{M+1}}{M}$ and $\pm\frac{2^{\frac{e}{2}}\sqrt{M+1}}{M}$, respectively. For the cases when the cross-correlation difference is 0, the autocorrelation terms dominate, and the resulting sidelobes at integer multiples of T_c with a level –108 dB corresponding to $-1/M$ are visible.

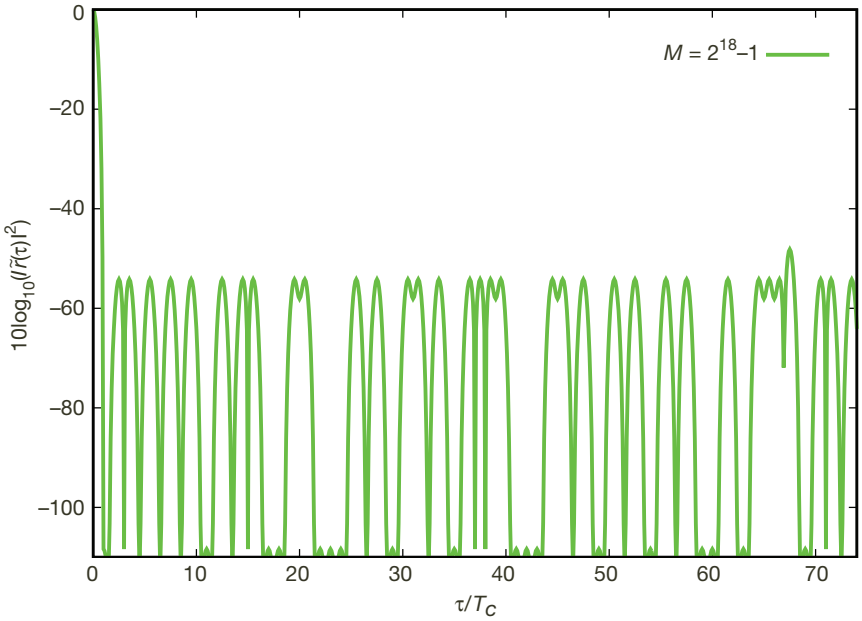

Figure 7. Autocorrelation of a complex baseband MSK waveform using a preferred pair of m-sequences, represented by the linear feedback shift registers 0*x*404A1 and 0*x*40081, with length $M = 2^{18}–1$.

Another option to generate the two sequences is to use offset periods of a single m-sequence. For the in-phase channel, use the m-sequence with no offset into the code sequence, and on the quadrature channel use the m-sequence offset by a fraction of the period. In this case, the auto and cross-correlation functions of the sequences will be two-valued:

$$\alpha_k = \begin{cases} M & k \bmod M - 0 \\ -1 & \text{otherwise,} \end{cases}$$

$$\beta_k = \begin{cases} M & k = K \bmod M \\ -1 & \text{otherwise.} \end{cases}$$

where K is the offset into the sequence for the quadrature channel

$$c_k^{(q)} = c_{k-K}^{(i)}. \tag{9}$$

To determine the offset, K, we again consider the region outside the main lobe, $|\tau| > T_c$, where the cross-correlation terms will dominate, with local maximum values occurring at odd multiples of half the chip time:

$$\tau = \frac{2m+1}{T_c} \quad m = \pm 1, \pm 2, \pm 3 \cdots.$$

The peak sidelobe values of the autocorrelation occurring at these delays, from Equation (8), are

$$\tilde{r}\left(l, \frac{T_c}{2}\right) \approx \frac{j}{2M}(\beta_{l+1} - \beta_{-l-2}) \quad l \in \left\{-\frac{M}{2}, \cdots, -2, 1, 2, \cdots \frac{M}{2} - 1\right\}.$$

The cross-correlation difference, $\beta_{l+1} - \beta_{-l-2}$, will be zero for all l except when $l + 1 = K$ or $(-l-2) \bmod M = K$, where the difference could evaluate to $\pm(M+1)$. If, however, we choose K such that both

$$l + 1 = K$$

and

$$(-l-2) \bmod M = K$$

are satisfied, then $\beta_{l+1} - \beta_{-l-2} = 0$ for all l. Writing $(-l-2) \bmod M$ as $M - l - 2$ and solving for K, an offset of $K = \frac{M-1}{2}$ will cancel the cross-correlation contributions, reducing the autocorrelation of the complex baseband waveform, Equation (7), to

$$\tilde{r}(l, \hat{\tau}) = \frac{\alpha_l}{M}\rho(T_c - \hat{\tau}) + \frac{\alpha_{l+1}}{M}\rho(\hat{\tau}) \quad 0 \le \hat{\tau} < T_c \quad l \in [-\frac{M}{2}, \frac{M}{2}).$$

For $|\tau| > T_c$, the sidelobe structure will have local maximum values occurring at integer multiples of T_c:

$$\tau = mT_c \quad m = \pm 1, \pm 2, \pm 3 \cdots.$$

The peak sidelobe values of the autocorrelation in this region are given by

$$\tilde{r}(l,T_c) = -\frac{1}{M} \quad l \in \left\{-\frac{M}{2}+1,\cdots,-2,1,2,\cdots\frac{M}{2}-2\right\}.$$

Local minima will occur at odd integer multiples of $T_c/2$,

$$\tau = \frac{2m+1}{T_c} \quad m = \pm 1, \pm 2, \pm 3\cdots,$$

giving

$$\tilde{r}\left(l,\frac{T_c}{2}\right) = -\frac{2}{M\pi} \quad l \in \left\{-\frac{M}{2}+1,\cdots,-2,1,2,\cdots\frac{M}{2}-2\right\}.$$

The use of a pair of codes, generated from a single m-sequence with a code offset of $\frac{M-1}{2}$ between the in-phase and quadrature-phase, can thus achieve both ideal auto and cross-correlation properties when used in this configuration; there will be no further consideration of using a preferred pair of m-sequences.

Consider using a sequence length of $M = 2^{18} - 1$, and the m-sequence represented by the linear-feedback shift register $0x404A1$. The magnitude square of the autocorrelation of the complex baseband signal, $\tilde{r}(\tau)$, is shown in Figures 8(a) and 8(b) for delays near zero and at half the period, respectively. The peak sidelobe levels of –108 dB occurring every integer multiple of T_c, corresponding to $-1/M$ and the minimum sidelobe levels of –112 dB every odd integer multiple of $T_c/2$, corresponding to $-\frac{2}{M\pi}$, are evident in both plots. In Figure 8(b), the magnitude square of the autocorrelation for a domain about $\tau = \frac{MT_c}{2}$ is shown, demonstrating the cross-correlation cancellation due to the choice of code offset $K = \frac{M-1}{2}$.

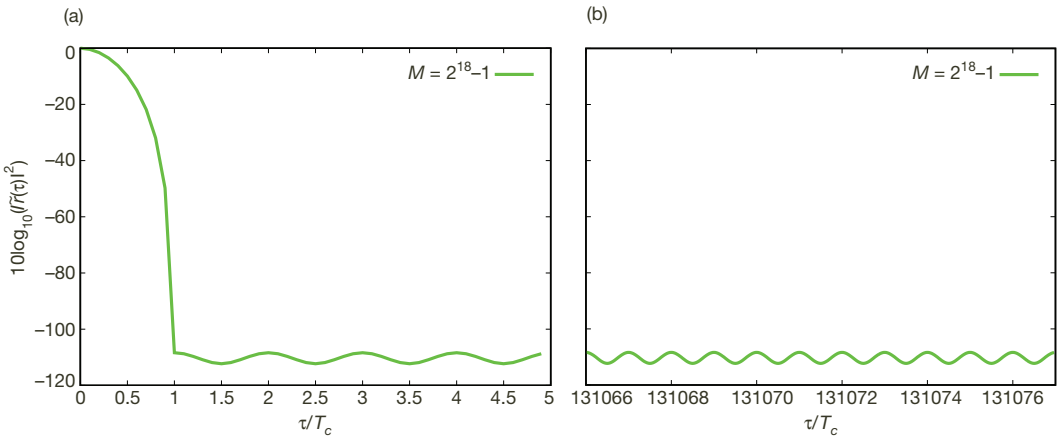

Figure 8. The autocorrelation of the complex baseband MSK waveform generated using a single m-sequence with an offset period of $K = (M-1)/2$, where $M = 2^{18}-1$: (a) $|\tau| \leq 75T_c$; (b) $(M-5)/2T_c \leq \tau \leq (M+5)/2T_c$.

C. Spectrum

The PSD of a waveform, $S(\omega)$, is given by the Fourier transform of its autocorrelation, $r(\tau)$. Representing the periodic waveform in terms of its Fourier series, solving for the autocorrelation, and then taking the Fourier transform, we have

$$S(\omega) = \frac{1}{4}F(\omega - \omega_c) + \frac{1}{4}F^*(-\omega - \omega_c),$$

where

$$F(\omega) = \sum_{k=-\infty}^{\infty} |a_k|^2 2\pi\delta\left(\omega + \frac{2\pi}{MT_c}k\right)$$

with

$$|a_k|^2 = \frac{4}{M^2\pi^2}\frac{\cos^2\left(\frac{\pi k}{M}\right)}{\left(1-\left(\frac{2k}{M}\right)^2\right)^2}\left|e^{j\frac{\pi k}{M}}\sum_{n=0}^{M-1} c_n^{(i)} e^{-j\frac{2\pi}{M}nk} - j\sum_{m=0}^{M-1} c_m^{(q)} e^{-j\frac{2\pi}{M}mk}\right|^2.$$

Using Parseval's relation, an upper bound to $|a_k|^2$ can be obtained, giving

$$|a_k|^2 \le \begin{cases} 2 & k = 0 \\ 2(M+1) & k = \pm 1, \pm 2, \cdots. \end{cases} \tag{10}$$

The spectrum is composed of spectral lines spaced at harmonics of the waveform repetition rate. As the period of the waveform increases, the spacing of these harmonics becomes closer, and their associated power decreases. The main lobe bandwidth of the waveform is $B = \frac{3}{T_c}$ Hz, and the spectral sidelobes decay more quickly than those of a corresponding BPC waveform.

Figure 9 contains a plot of the power of the waveform in 1-Hz increments for a signal with a period $M = 2^{18} - 1$ using the m-sequence formed by the linear feedback shift register $0x40081$, and a chip time $T_c = 0.075\ \mu$s; the curve formed from the PSD and a curve formed from the bound Equation (10) are shown. The main lobe bandwidth is $B = \frac{3}{T_c} = 40$ MHz.

D. Ambiguity Function

The ambiguity function of a signal with period T is defined as

$$\xi(\tau, f_d) \triangleq \frac{1}{T}\int_{-T/2}^{T/2} z(t)z(t+\tau)e^{j2\pi f_d t}dt \quad -T/2 \le \tau < T/2.$$

Evaluating this with Equation (3), and defining τ in terms of l integer multiples of T_c and a residual $\hat{\tau}$,

$$l = \left\lfloor \frac{\tau}{T_c} \right\rfloor \quad \hat{\tau} = \tau - lT_c,$$

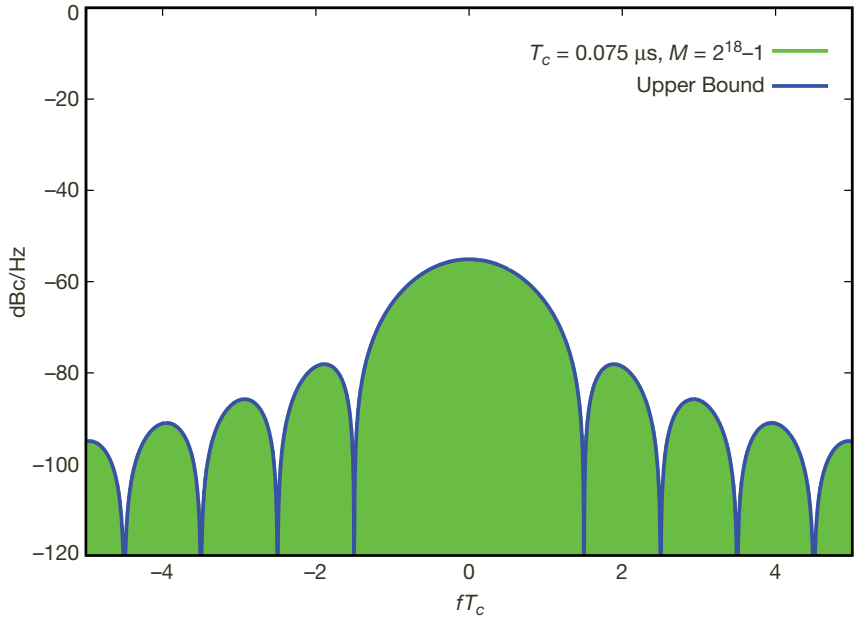

Figure 9. The spectral power in 1-Hz intervals for an MSK waveform with T_c = 0.075 µs and $M = 2^{18}–1$.

we have

$$\xi(l,\hat{\tau},f_d) = \frac{1}{2}\Re\left\{\tilde{\xi}(l,\hat{\tau},f_d)e^{j\omega_c\tau}\right\} \quad -T/2 \le \tau < T/2,$$

where

$$\tilde{\xi}(l,\hat{\tau},f_d) = \begin{cases} \dfrac{e^{-j\pi f_d\hat{\tau}}}{2M}\Big[\gamma(T_c-\hat{\tau},f_d\alpha_l^{(i)} + \gamma(\hat{\tau},f_d)e^{j\pi f_d T_c}\alpha_{l+1}^{(i)} \\ +\gamma(T_c-\hat{\tau},f_d)e^{j\pi f_d T_c}\alpha_l^{(q)} + \gamma(\hat{\tau},f_d)e^{j\pi f_d 2T_c}\alpha_{l+1}^{(q)} \\ -j\gamma\left(\dfrac{T_c}{2}-\hat{\tau},f_d\right)e^{j\pi f_d\frac{T_c}{2}}\beta_l^{(q,i)} - j\gamma\left(\dfrac{T_c}{2}+\hat{\tau},f_d\right)e^{j\pi f_d\frac{3T_c}{2}}\beta_{l+1}^{(q,i)} \\ +j\gamma\left(\dfrac{T_c}{2}-\hat{\tau},f_d\right)e^{-j\pi f_d\frac{T_c}{2}}\beta_{l-1}^{(i,q)} + j\gamma\left(\dfrac{T_c}{2}+\hat{\tau},f_d\right)e^{j\pi f_d\frac{T_c}{2}}\beta_l^{(i,q)}\Big] & 0 \le \hat{\tau} < \dfrac{T_c}{2} \\ \dfrac{e^{-j\pi f_d\hat{\tau}}}{2M}\Big[\gamma(T_c-\hat{\tau},f_d)\alpha_l^{(i)} + \gamma(\hat{\tau},f_d)e^{j\pi f_d T_c}\alpha_{l+1}^{(i)} \\ +\gamma(T_c-\hat{\tau},f_d)e^{j\pi f_d T_c}\alpha_l^{(q)} + \gamma(\hat{\tau},f_d)e^{j\pi f_d 2T_c}\alpha_{l+1}^{(q)} \\ -j\gamma\left(\dfrac{3T_c}{2}-\hat{\tau},f_d\right)e^{j\pi f_d\frac{3T_c}{2}}\beta_{l+1}^{(q,i)} - j\gamma\left(\hat{\tau}-\dfrac{T_c}{2},f_d\right)e^{j\pi f_d\frac{5T_c}{2}}\beta_{l+2}^{(q,i)} \\ +j\gamma\left(\dfrac{3T_c}{2}-\hat{\tau},f_d\right)e^{j\pi f_d\frac{T_c}{2}}\beta_l^{(i,q)} + j\gamma\left(\hat{\tau}-\dfrac{T_c}{2},f_d\right)e^{j\pi f_d\frac{3T_c}{2}}\beta_{l+1}^{(i,q)}\Big] & \dfrac{T_c}{2} \le \hat{\tau} < T_c \end{cases}$$

with

$$\gamma(\tau,f_d) \triangleq \begin{cases} -\dfrac{\cos\left(\dfrac{\pi}{T_c}\tau\right)\sin(\pi f_d \tau)}{\pi f_d T_c} + \dfrac{\sin\left(\pi\left(\dfrac{1}{T_c}+f_d\right)\tau\right)}{2\pi\left(\dfrac{1}{T_c}+f_d\right)T_c} + \dfrac{\sin\left(\pi\left(-\dfrac{1}{T_c}+f_d\right)\tau\right)}{2\pi\left(-\dfrac{1}{T_c}+f_d\right)T_c} & f_d \neq 0 \\ -\cos\left(\dfrac{\pi\tau}{T_c}\right)\dfrac{\tau}{T_c} + \dfrac{1}{\pi}\sin\left(\dfrac{\pi\tau}{T_c}\right) & f_d = 0, \end{cases}$$

$$\alpha_k^{(i)} \triangleq \sum_{n=0}^{M-1} c_n^{(i)} c_{n+k}^{(i)} e^{j2\pi f_d T_c n}, \quad \alpha_k^{(q)} \triangleq \sum_{n=0}^{M-1} c_n^{(q)} c_{n+k}^{(q)} e^{j2\pi f_d T_c n},$$

$$\beta_k^{(i,q)} \triangleq \sum_{n=0}^{M-1} c_n^{(i)} c_{n+k}^{(q)} e^{j2\pi f_d T_c n}, \quad \text{and} \quad \beta_k^{(q,i)} \triangleq \sum_{n=0}^{M-1} c_n^{(q)} c_{n+k}^{(i)} e^{j2\pi f_d T_c n}.$$

Assuming the code sequences $\{c_n^{(i)}\}$ and $\{c_n^{(q)}\}$ are generated from a single m-sequence, with a period offset, Equation (9), of $K = \frac{M-1}{2}$ and $f_d << \frac{\sqrt{M}}{T}$, the cross-correlation terms cancel, giving

$$\tilde{\tilde{\xi}}(l,\hat{\tau},f_d) = \frac{e^{-j\pi f_d \hat{\tau}}}{2M}\left[\gamma(T_c-\hat{\tau},f_d)\alpha_l^{(i)} + \gamma(\hat{\tau},f_d)e^{j\pi f_d T_c}\alpha_{l+1}^{(i)} + \gamma(T_c-\hat{\tau},f_d)e^{j\pi f_d T_c}\alpha_l^{(q)} + \gamma(\hat{\tau},f_d)e^{j\pi f_d 2T_c}\alpha_{l+1}^{(q)}\right]$$
$$0 \le \hat{\tau} < T_c \quad l \in \left[-\frac{M}{2},\frac{M}{2}\right).$$

To determine the domain of Doppler offsets that can be effectively detected, we consider the 1 dB extent of the ambiguity function on the Doppler axis at $\tau = 0$. Setting $\hat{\tau} = 0$ and $l = 0$, the ambiguity function reduces to

$$\tilde{\tilde{\xi}}(0,0,f_d) \approx e^{j\pi f_d T_c\left(M-\frac{1}{2}\right)}\left[\frac{\sin(\pi f_d T_c)}{\pi f_d T_c} + \frac{\sin(\pi(f_d T_c+1))}{2\pi(f_d T_c+1)} + \frac{\sin(\pi(f_d T_c-1))}{2\pi(f_d T_c-1)}\right]\cos\left(\pi\frac{f_d T_c}{2}\right)\frac{\sin(\pi f_d M T_c)}{\pi f_d M T_c}.$$

For $f_d << \frac{\sqrt{M}}{T}$, the $sin(x)/x$ response with the first null occurring at $f_d = 1/(MT_c)$ dominates. Using the 1 dB extent of the main lobe as the effective Doppler domain, Doppler shifts within

$$-\frac{1}{4MT_c} \le f_d \le \frac{1}{4MT_c}$$

are detectable. Relating this to the bandpass signal, the effective Doppler bandwidth is

$$B_{D_{eff}} = \frac{1}{2MT_C}.$$

To find the peak ambiguity function sidelobe, in delay and Doppler, we take the magnitude of the complex baseband ambiguity function evaluated at $\hat{\tau} = T_c$:

$$|\tilde{\tilde{\xi}}(l,T_c,f_d)| = \frac{1}{2M}\left|\gamma(0,f_d)\left(\alpha_l^{(i)} + e^{j\pi f_d T_c}\alpha_l^{(q)}\right) + \gamma(T_c,f_d)\left(e^{j\pi f_d T_c}\alpha_{l+1}^{(i)} + e^{j\pi f_d 2T_c}\alpha_{l+1}^{(q)}\right)\right|$$
$$\le \frac{1}{2M}\left|\left(\alpha_l^{(i)} + e^{j\pi f_d T_c}\alpha_l^{(q)}\right)\right|.$$

For the region outside the main lobe, $l \neq \{-1, 0, 1\}$ and $f_d \neq 0$, it can be shown, using Parseval's relation, that for an m-sequence, $\{c_n\}$,

$$\left| \sum_{n=0}^{M-1} c_n c_{n+1+l} e^{j2\pi f_d (n+1) T_c} \right|^2 \approx M + 1.$$

Applying this approximation, we have

$$|\tilde{\xi}(l, T_c, f_d)| \leq \frac{1}{2M} \sqrt{\left| \alpha_l^{(i)} + e^{j\pi f_d T_c} \alpha_l^{(q)} \right|^2} = \sqrt{\frac{M+1}{M^2}} \approx \frac{1}{\sqrt{M}} \qquad l \neq \{-1, 0, 1\} \quad f_d \neq 0.$$

The peak ambiguity function sidelobe is therefore given by

$$\tilde{\xi}_{peak} = \frac{1}{\sqrt{M}}.$$

The magnitude square of the ambiguity function of the complex baseband signal is plotted in Figure 10 and Figure 11 for the MSK waveform with $T_c = 0.075\ \mu s$ and a code period $M = 2^{18} - 1$ generated from the linear feedback shift register $0x40081$. In Figure 10, a domain encompassing the main lobe is shown in order to demonstrate the main lobe and peak sidelobe structure of the function. Considering the main lobe, the delay resolution of $\Delta_{6\,dB} = 0.8T_c$ is evident along with the effective Doppler resolution of $B_{D_{eff}} = \frac{1}{2T}$. Outside of the main lobe, the peak sidelobes of –54 dB dominate. In Figure 10, a domain in the vicinity of $\tau = \frac{M-1}{2} T_c$ is shown to demonstrate the cross-correlation cancellation at a delay corresponding to the code sequence period offset $\frac{M-1}{2}$.

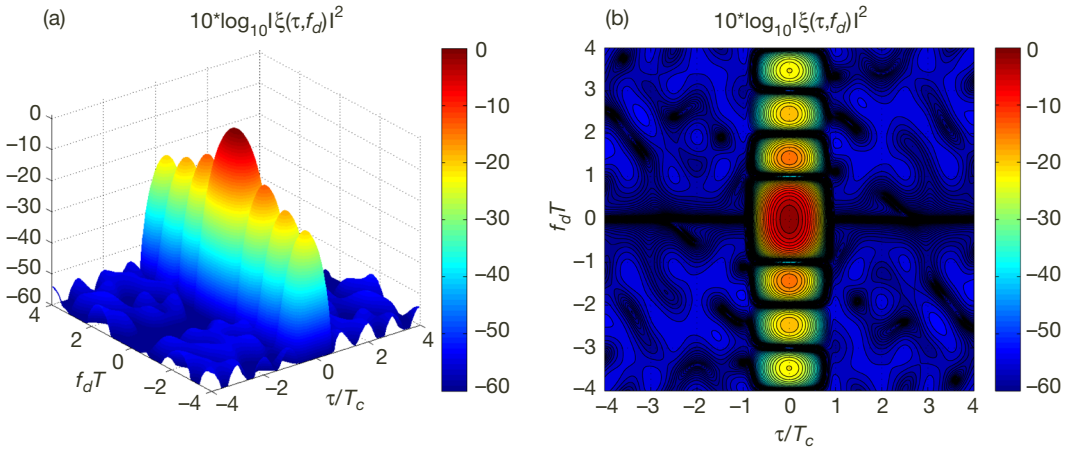

Figure 10. The ambiguity function of the complex baseband MSK waveform, generated using a single m-sequence of length $M = 2^{18}–1$ with offset $K = 0$ for the in-phase and $K = (M–1)/2$ for the quadrature-phase sequence, encompassing the main lobe: (a) 3-d plot; (b) contour plot.

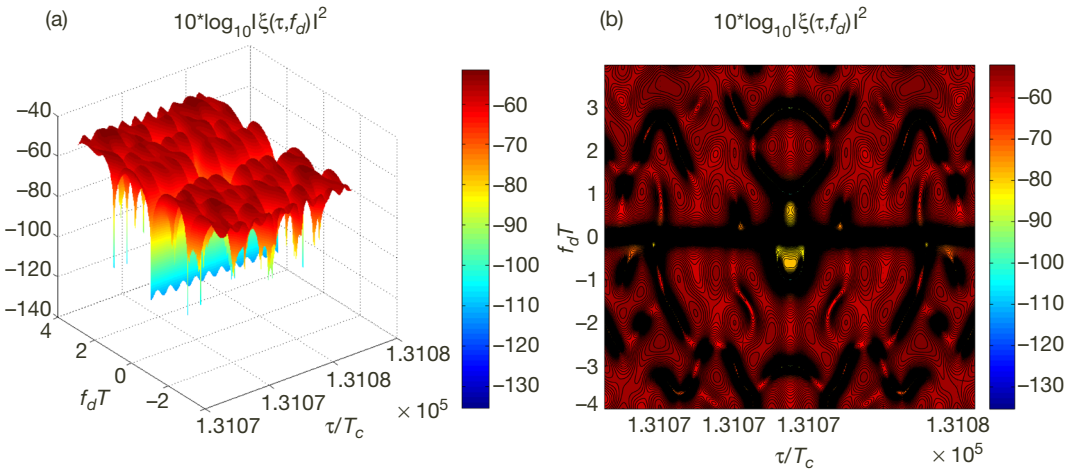

Figure 11. The ambiguity function of the complex baseband MSK waveform, generated using a single m-sequence of length $M = 2^{18}–1$ with offset $K = 0$ for the in-phase and $K = (M–1)/2$ for the quadrature-phase sequence, about $\tau = (M–1)/2T_c$: (a) 3-d plot; (b) contour plot.

E. Waveform Characteristics Summary

For the MSK waveform with a main lobe bandwidth B and a period T, the waveform characteristics are summarized in terms of these parameters (Table 2):

Table 2. Summary of MSK waveform characteristics.

Unambiguous Delay Depth	T
Delay Resolution	$\Delta_{3\,dB} = \frac{1.68}{B}$ $\Delta_{6\,dB} = \frac{2.4}{B}$
Unambiguous Doppler Bandwidth	$\frac{1}{T}$
Effective Doppler Bandwidth	$B_{D_{eff}} = \frac{1}{2T}$
Peak Ambiguity Sidelobe	$\xi_{peak} = \sqrt{\frac{3}{BT}}$

V. Costas F-H Waveform

The Costas-FH waveform is described, and an analysis of the waveform's autocorrelation, spectrum, and ambiguity functions is performed. A summary of the waveform characteristics in terms of the duration and bandwidth of the waveform is given.

A. Waveform

An FH waveform is generated by dividing the allocated bandwidth B into N frequencies, and then transmitting the sequence of frequencies in some predetermined order, dwelling at each for a duration of T_p seconds, so that one period of the FH waveform is $T = NT_p$, as

shown in Figure 12. The bandpass waveform is formed by periodically modulating this pattern onto an RF carrier, giving us

$$z(t) = \Re\left\{ \sum_{k=-\infty}^{\infty} x(t - kT) e^{j\omega_c t} \right\},$$

where $x(t)$ is given by

$$x(t) = \sum_{n=0}^{N-1} p(t - nT_p) e^{-j\omega_n t}.$$

Here, $p(t)$ is a rectangular pulse of duration T_p, and the nth hop frequency is $\omega_n = 2\pi\theta_n / T_p$, where the hop pattern, $\{\theta_n\}$, is a permutation of the integers $\{0, 1, \ldots, N-1\}$. In order to minimize range-Doppler ambiguity, the frequency hop pattern is chosen from among the class of Costas codes [5]. Note that the Costas code is repeated cyclically in this application, which differs from the usage in [5]. The number of hops, N, is completely determined by noting that the separation between adjacent frequencies is $\Delta f = 1/T_p$, so that the total bandwidth is $B = N\frac{1}{T_p}$ and that $T = NT_p$, leading to the relationship

$$N = \sqrt{BT}.$$

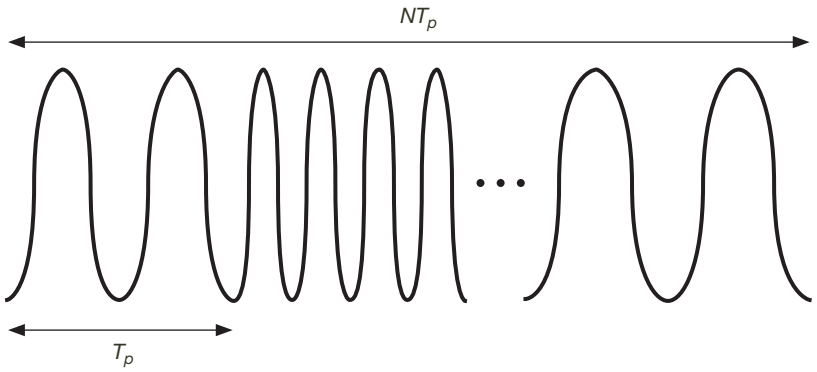

Figure 12. FH waveform with *N* frequencies and a duration NT_p.

B. Autocorrelation

The autocorrelation function of $z(t)$ is periodic, with a single period given by

$$r(\tau) = \frac{1}{2}\Re\left\{\tilde{r}(\tau) e^{j\omega_c \tau}\right\} \quad -\frac{T}{2} < \tau \leq \frac{T}{2},$$

where $\tilde{r}(\tau)$ is the complex baseband autocorrelation function. Letting $\tau = lT_p + \hat{\tau}, 0 \leq \hat{\tau} < T_p$, i.e., $l = \left\lfloor \frac{\tau}{T_p} \right\rfloor$ and $\hat{\tau} = \tau - lT_p$, we can write

$$\tilde{r}(\tau) = \tilde{r}(l,\hat{\tau})$$
$$= \begin{cases} \dfrac{T_p - |\hat{\tau}|}{NT_p} e^{j\pi(N-1)|\hat{\tau}|/T_p} \dfrac{\sin\left(N\pi|\hat{\tau}|/T_p\right)}{\sin\left(\pi|\hat{\tau}|/T_p\right)} + \dfrac{|\hat{\tau}|}{NT_p} \displaystyle\sum_{n=0}^{N-1} e^{j\pi(\theta_n+\theta_{n+1})|\hat{\tau}|/T_p} \operatorname{sinc}\left((\theta_{n+1}-\theta_n)|\hat{\tau}|/T_p\right) & l=-1,0 \\ \dfrac{\hat{\tau}}{T} \displaystyle\sum_{n=0}^{N-1} \left(\operatorname{sinc}((\theta_{n+l+1}-\theta_n)\hat{\tau}/T_p) e^{j\pi(\theta_n+\theta_{n+l+1})\hat{\tau}/Tp} - \operatorname{sinc}((\theta_{n+l}-\theta_n)\hat{\tau}/T_p) e^{j\pi(\theta_n+\theta_{n+l})\hat{\tau}/Tp}\right) & \text{otherwise.} \end{cases}$$

Note that as the frequency hop pattern is periodic, $\theta_n = \theta_{n \bmod N}$.

If we consider the region $|\tau| < T_p$, then $l = 0$, and the magnitude of the autocorrelation is approximated as

$$|\tilde{r}(0,\hat{\tau})| \approx \left|\frac{T_p - \hat{\tau}}{T_p} \frac{\sin(N\pi\hat{\tau}/T_p)}{N\sin(\pi\hat{\tau}/T_p)}\right|,$$

which has sidelobe nulls occurring at

$$\hat{\tau} = n\frac{T_p}{N}, \quad n = \pm 1, \pm 2, \cdots$$

and sidelobe peaks at

$$\hat{\tau} = (2n+1)\frac{T_p}{2N}, \quad \pm 1, \pm 2, \cdots.$$

The first sidelobe thus has a level of –13.4 dB with respect to the peak, independent of the value of N. Figure 13 shows the magnitude square of the autocorrelation function when T_p = 17.25 μs and N = 690. Note that Figure 13(b) shows that away from the main lobe ($\tau > T_p$), the autocorrelation peaks do not exceed $2/N$, or approximate –50 dB, with N = 690, in power relative to the center peak, as expected for Costas codes [5].

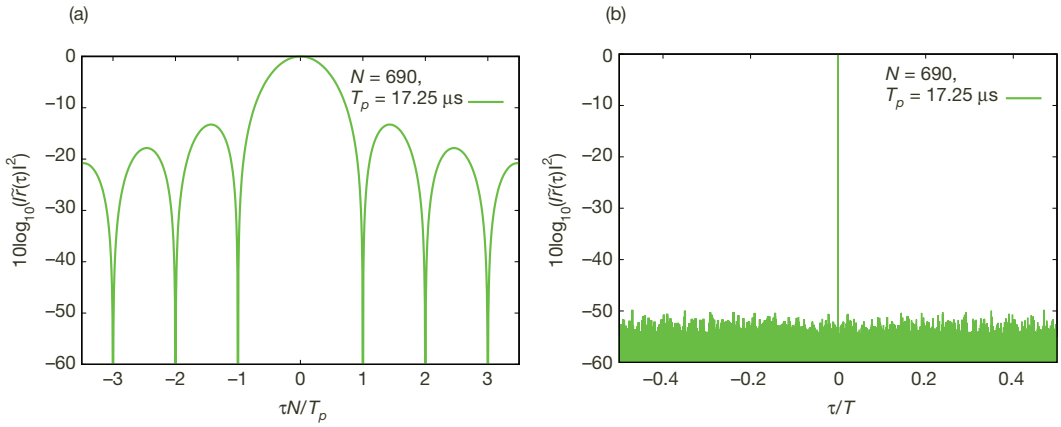

Figure 13. FH waveform autocorrelation function with Costas code, N = 690, T_p = 17.25 μs: (a) $\tau << T_p$; (b) entire period.

The delay resolution, defined by the 6 dB and 3 dB widths of the autocorrelation main lobe, is approximately

$$\Delta_{6\,dB} = 1.2\frac{T_p}{N}$$

and

$$\Delta_{3\,dB} = 0.88\frac{T_p}{N}.$$

C. Spectrum

The PSD of $z(t)$ is given by

$$S(\omega) = \frac{1}{4}F(\omega - \omega_c) + \frac{1}{4}F^*(-\omega - \omega_c),$$

where $F(\omega)$ is the Fourier transform of the autocorrelation of the complex baseband waveform, given by

$$F(\omega) = \sum_{k=-\infty}^{\infty} |a_k|^2 2\pi\delta\left(\omega + \frac{2\pi}{MT_c}k\right)$$

and the Fourier series coefficients of the baseband waveform are given by

$$a_k = \frac{2}{T}e^{-j\pi k/N}\sum_{n=0}^{N-1} e^{j\pi\theta_n T_p}e^{j2\pi n\theta_n T_p}e^{-j2\pi nk/N}\frac{\sin(\frac{\pi k}{N} - \pi\theta_n T_p)}{\frac{2\pi k}{T} - 2\pi\theta_n}.$$

Figure 14 shows a plot of the power spectrum for T_p = 17.25 μs and N = 690 where the origin has been shifted by $-\frac{N}{2T_p}$.

D. Ambiguity Function

The ambiguity function of a signal with period T is defined as

$$\begin{aligned}\xi(\tau, f_d) &\triangleq \frac{1}{T}\int_{-T/2}^{T/2} z(t)z(t+\tau)e^{j2\pi f_d t}dt \quad -T/2 \le \tau < T/2 \\ &= \frac{1}{2}\Re\left\{\tilde{\xi}(\tau, f_d)e^{j\omega_c\tau}\right\}.\end{aligned}$$

Again letting $l = \left\lfloor\frac{\tau}{T_p}\right\rfloor$ and $\hat{\tau} = \tau - lT_p$, we can write the ambiguity function of the baseband FH waveform as

$$\begin{aligned}\tilde{\xi}(l, \hat{\tau}, f_d) = &\frac{1}{NT_p}\sum_{n=0}^{N-1}\frac{e^{j2\pi(f_d(n+1)T_p + (f_n - f_d)\hat{\tau})} - e^{j2\pi(f_d nT_p + f_{n+l}\hat{\tau})}}{j2\pi(f_d + f_{n+l} - f_n)} \\ &+ \frac{1}{NT_p}\sum_{n=0}^{N-1}\frac{e^{j2\pi(f_d(n+1)T_p + f_{n+l+1}\hat{\tau})} - e^{j2\pi(f_d(n+1)T_p + (f_n - f_d)\hat{\tau})}}{j2\pi(f_d + f_{n+l+1} - f_n)},\end{aligned}$$

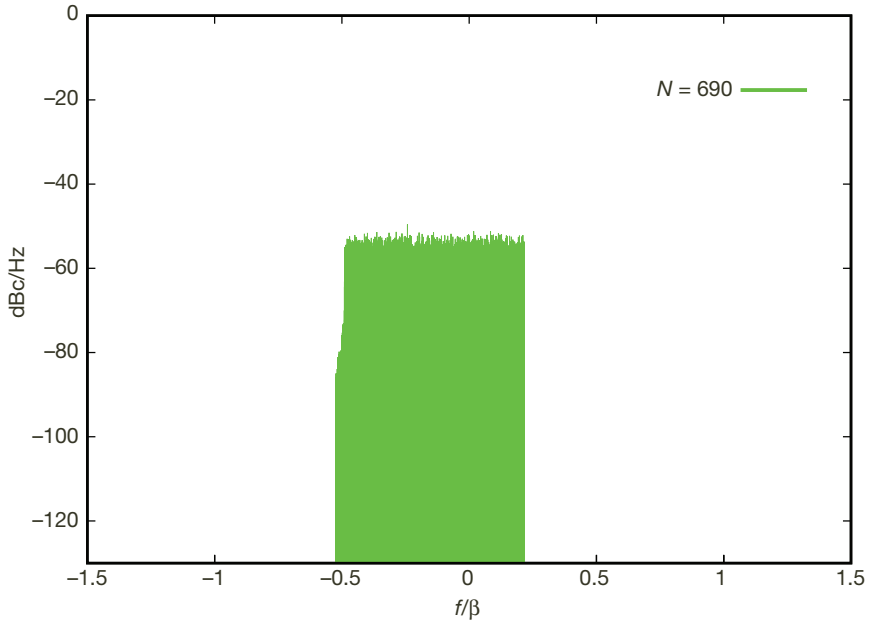

Figure 14. The spectral power in 1-Hz intervals for an FH waveform with Costas code $N = 690$, $T_p = 17.25$ µs.

where $f_n = \frac{\omega_n}{2\pi}$. The behavior of this function along the delay axis ($f_d = 0$) is described in the autocorrelation section. On the other hand, when $\tau = 0$, the magnitude of the ambiguity function is

$$|\tilde{\tilde{\xi}}(0,f_d)| = \text{sinc}(f_d N T_p).$$

So along the Doppler axis, the sidelobe nulls occur at

$$f_d = \frac{n}{NT_p} \quad n = \pm 1, \pm 2, \cdots,$$

and the sidelobe peaks occur at

$$f_d = \frac{2n+1}{2NT_p} \quad \pm 1, \pm 2, \cdots.$$

The effective Doppler domain is defined as the 1-dB extent of the main lobe of the ambiguity function along the Doppler axis at a delay of $\tau = 0$, and is given by

$$B_{D_{eff}} = \frac{1}{2NT_p} Hz.$$

A plot of the magnitude square of the ambiguity function near the central peak is shown in Figure 15. The sinc function structure is evident from this figure, with its high peak sidelobe level of –13.4 dB. The delay resolution of 0.88 T_p/N and effective Doppler resolution of $0.5/T$ are evident from Figure 15 as well. The ambiguity peaks far from the main lobe are not visible in this figure; however, we conjecture that their values are the same as those of the standard Costas ambiguity function described in [5], i.e., $2/N$.

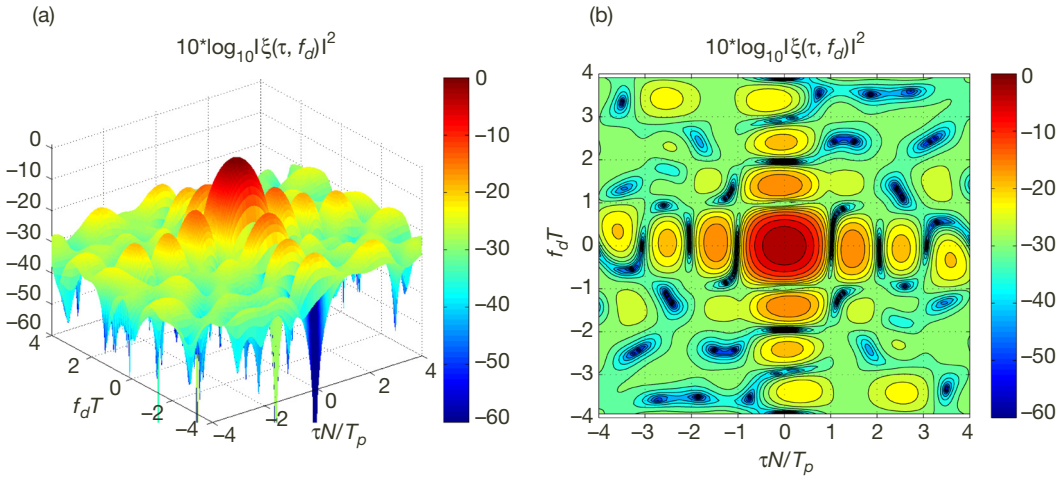

Figure 15. Ambiguity function of FH waveform with Costas code, $N = 690$, $T_p = 17.25$ µs, $\tau << T_p$: (a) 3-d plot; (b) contour plot.

E. Windowing

The relatively high ambiguity function sidelobe levels, starting at –13.4 dB, can be reduced through the use of windowing functions. In spectral analysis, one often applies a window function to the time series to reduce the spectral sidelobes, which allows the identification of spectra with large dynamic ranges [10]. The dual technique can be applied to reduce the time domain sidelobes by applying a window function to the frequency response of the waveform. This will result in a reduction of the ambiguity function sidelobes at the expense of a wider main lobe and resulting loss in resolution. As we wish to maintain the constant envelope properties of the transmitted signal, the windowed frequency response cannot be split between the transmitted waveform and received correlator. This will result in a loss in the signal-to-noise ratio (SNR) as the receiver will no longer be matched to the transmitted waveform. Several options are available, including Taylor and Hamming window functions, that will reduce the peak sidelobe to less than –40 dB at the cost of less than 1.5 dB in SNR and an increase in the main lobe width, degrading the resolution by at most 150 percent [11, p. 345] [3, pp. 612–618]. We now verify this for the frequency-hopping case by using a Hamming window and analyzing the effect upon the autocorrelation function.

As shown earlier, in the region $\tau << T_p$, the autocorrelation function may be approximated as

$$\tilde{r}(\tau) \approx e^{j\pi(N-1)\tau/T_p}\,\mathrm{sinc}(N\tau/T_p).$$

If we apply a Hamming window with frequency response

$$H(f) = 0.08 + 0.92\cos^2(\pi f T_p/N), \quad |f| \leq \frac{N}{2T_p} \tag{11}$$

to the received signal in the frequency domain, then the windowed autocorrelation function $\tilde{r}_w(\tau)$ will be given by

$$
\begin{aligned}
\tilde{r}_w(\tau) &= \mathcal{F}^{-1}\left\{\mathcal{F}\{\tilde{r}_w(\tau)\}H\left(f+\frac{N}{2T_p}\right)\right\} \\
&= \mathcal{F}^{-1}\left\{\frac{T_p}{N}\,\mathrm{rect}\left(\frac{T_p}{N}f+\frac{1}{2}\right)H\left(f+\frac{N}{2T_p}\right)\right\} \\
&= \frac{T_p}{N}\int_{-\frac{N}{2T_p}}^{\frac{N}{2T_p}}\left(0.08+0.92\cos^2(\pi f T_p/N)\right)e^{j2\pi f\tau}\,df \\
&= \left(0.08+\frac{0.46}{1-\left(\frac{N\tau}{T_p}\right)^2}\right)\mathrm{sinc}\left(\frac{N\tau}{T_p}\right),
\end{aligned}
\tag{12}
$$

where $\mathcal{F}$ denotes the Fourier transform. This windowed autocorrelation function is plotted along with the original function in Figure 16. We see that the first sidelobes are reduced to –43.5 dB with respect to the peak, while the main lobe is broadened at the 6 dB point to approximately 1.8 T_p/N, a factor of 1.5 increase. The SNR loss can be calculated from

$$
\begin{aligned}
\Delta_{SNR} &= \frac{|\tilde{r}_w(0)|^2}{\int_{-\infty}^{\infty}|H(f)|^2\,df} \\
&= \frac{(0.08+0.46)^2}{0.4} \\
&= -1.34\ dB.
\end{aligned}
\tag{13}
$$

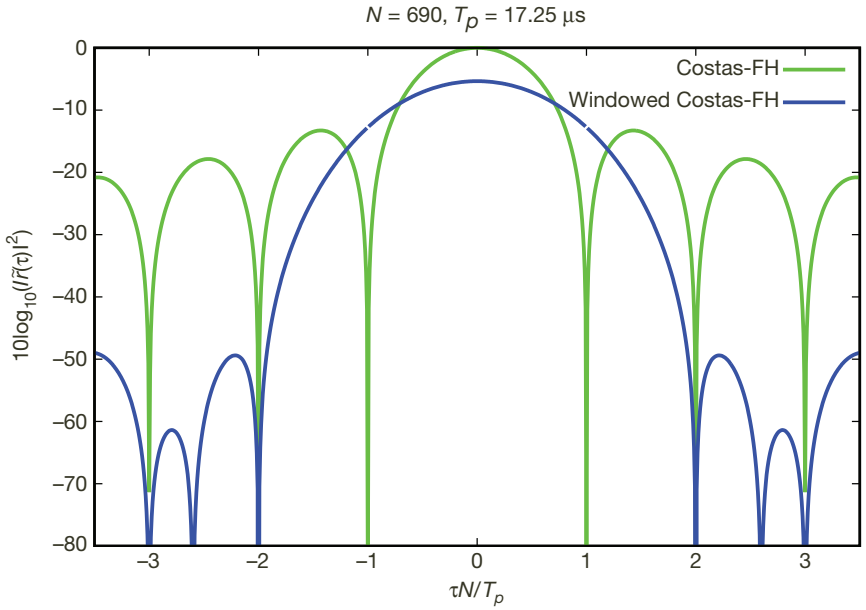

Figure 16. FH autocorrelation function with and without Hamming window, $N = 690$, $T_p = 17.25$ µs.

F. Waveform Characteristics Summary

For the Costas-FH waveform with main lobe bandwidth B and period T, the waveform characteristics are summarized in terms of these parameters for the standard and windowed cases (Table 3):

Table 3. Summary of Costas-FH waveform characteristics.

	Costas-FH	Windowed Costas-FH
Unambiguous Delay Depth	T	T
Delay Resolution	$\Delta_{3\,dB} = \frac{0.88}{B}$ $\Delta_{6\,dB} = \frac{1.2}{B}$	$\Delta_{3\,dB} = \frac{1.3}{B}$ $\Delta_{6\,dB} = \frac{1.8}{B}$
Unambiguous Doppler Bandwidth	$\frac{1}{T}$	$\frac{1}{T}$
Effective Doppler Bandwidth	$B_{D_{eff}} = \frac{1}{2T}$	—
Peak Ambiguity Sidelobe	$\xi_{peak} = -13.4$ dB	$\xi_{peak} = -43.5$ dB

Note that the effective Doppler bandwidth has not been given for the windowed Costas-FH case, as no closed-form expression has yet been obtained.

VI. LFM Waveform

The LFM waveform is described, and an analysis of the waveform's autocorrelation, spectrum, and ambiguity functions is performed. A summary of the waveform characteristics in terms of the duration and bandwidth of the waveform is given.

A. Waveform

The LFM waveform, also known as the chirp waveform, has a linearly increasing or decreasing frequency during the nonzero portion of the waveform, as shown in Figure 17. The transmitted signal, $z(t)$, is formed by periodically extending the waveform and modulating it onto an RF carrier. Writing the transmitted signal in terms of the complex baseband signal, we have

$$z(t) = \Re\left\{ \sum_{k=-\infty}^{\infty} x(t - kT) e^{j\omega_c t} \right\},$$

where

$$x(t) = e^{j\pi \frac{\beta}{T_p} t^2} \big(u(t) - u(t - T_p)\big),$$

$u(t)$ denotes the unit step function, T is the period of the waveform, T_p/T is the duty cycle of the waveform, and β/T_p is the rate of the frequency change. The waveform has a constant envelope and a continuous phase.

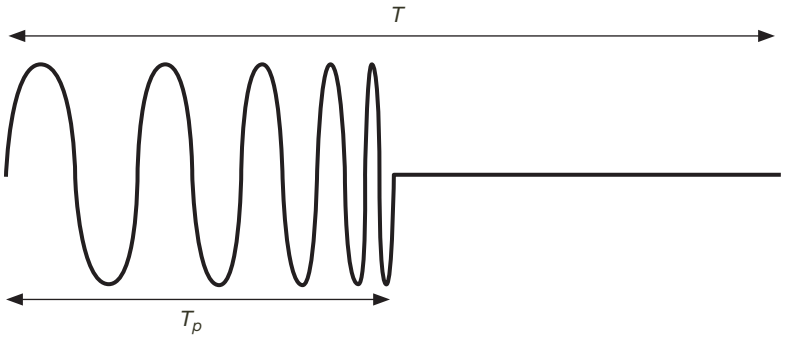

Figure 17. LFM waveform with a duty cycle of T_p/T and duration T.

B. Autocorrelation

The autocorrelation function of $z(t)$ is periodic; a single period is given by

$$\begin{aligned} r(\tau) &= \frac{1}{T}\int_{-T/2}^{T/2} z(t)z(t+\tau)dt \quad -T/2 \le \tau < T/2 \\ &= \frac{1}{2}\Re\left\{\tilde{r}(\tau)e^{j\omega_c\tau}\right\} \quad -T/2 \le \tau < T/2, \end{aligned} \tag{14}$$

where

$$\begin{aligned} \tilde{r}(\tau) = \rho(\tau+T)\big(u(\tau+T) - u(\tau+(T-T_p))\big) + \rho(\tau)\big(u(\tau+T_p) - u(\tau-T_p)\big) \\ + \rho(\tau-T)\big(u(\tau-(T-T_p)) - u(\tau-T)\big) \quad |\tau| \le T/2 \end{aligned}$$

with

$$\rho(\tau) \triangleq e^{-j\pi\beta\tau}\frac{(T_p - |\tau|)}{T}\frac{\sin\left(\pi\frac{\beta}{T_p}\tau(T_p - |\tau|)\right)}{\pi\frac{\beta}{T_p}\tau(T_p - |\tau|)}.$$

This is the superposition of truncated $sin(x)/x$-type responses centered at $-T$, 0, and T. The extent of each response is determined by the duty cycle of the waveform. For a duty cycle of less than 50 percent, there is no overlap between the responses; only a single response exists in $[-T/2, T/2]$. For a duty cycle of greater than 50 percent, the responses overlap; however, even in the case of 100 percent duty cycle, $T_p = T$, the overlap has contributions from sidelobes with levels less than

$$\frac{\sin\left(\pi\frac{\beta T}{4}\right)}{\pi\frac{\beta T}{4}},$$

which for $\beta T >> 1$ is negligible.

Examining Equation (14), we note the $sin(x)/x$ response with a peak value occurring at $\tau = 0$. For $\beta T_p >> 1$, the response is independent of the βT_p product, and we have sidelobe nulls occurring at

$$\frac{n}{\beta} \quad n = \pm 1, \pm 2, \cdots$$

and peaks occurring at

$$\frac{2n+1}{2\beta} \quad n = \pm 1, \pm 2, \cdots.$$

The first sidelobe will have a level at –13.4 dB with respect to the peak, and the subsequent sidelobes will decay as the inverse distance from the origin. For $\beta T_p >> 1$, the 3 dB and 6 dB widths of the main lobe are approximately $0.88/\beta$ and $1.2/\beta$, respectively. Using these as a measure of the delay resolution, we have

$$\Delta_{3\,dB} = \frac{0.88}{\beta}$$

and

$$\Delta_{6\,dB} = \frac{1.2}{\beta}.$$

The phase of the autocorrelation,

$$(\omega_c + \beta)\tau,$$

varies linearly in τ with a slope, excluding the carrier contribution, of β.

In Figures 18(a) and (b), the magnitude square of the autocorrelation of the complex baseband signal for an LFM waveform with a 100 percent duty cycle, $T_p = T$, and a βT_p product of 480000 as well as a waveform with a 10 percent duty cycle, $T_p = T/10$ and a βT_p product of 48000 are plotted. In Figure 18(a), the main lobe and several adjacent sidelobes are shown; note, as demonstrated in Equation (18), with $\beta T_p >> 1$ the responses differ only in their relative level, the 10 percent duty cycle being down by 20 dB. The entire unambiguous delay extent is shown in Figure 18(b); note the 10 percent duty cycle has support only for $|\tau| \leq T_p$.

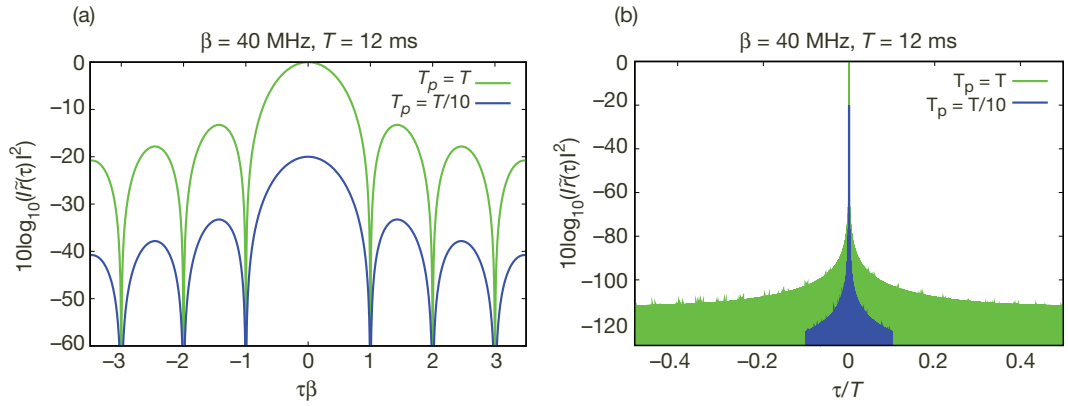

Figure 18. Autocorrelation of complex baseband LFM waveforms with β = 40 MHz, T = 12 ms, and duty cycles T_p/T = 1 and T_p/T = 0.1: (a) $|\tau| \leq 2\beta$; (b) entire period.

C. Spectrum

The PSD of a waveform, $S(\omega)$, is given by the Fourier transform of its autocorrelation, $r(\tau)$. Representing the periodic waveform in terms of its Fourier series, solving for the autocorrelation, and then taking the Fourier transform, we have

$$S(\omega) = \frac{1}{4}F(\omega - \omega_c) + \frac{1}{4}F^*(-\omega - \omega_c),$$

where

$$F(\omega) = \sum_{k=-\infty}^{\infty} |a_k|^2 2\pi\delta\left(\omega + \frac{2\pi}{T}k\right)$$

with

$$|a_k|^2 = \begin{cases} \frac{1}{T^2}\frac{T_p}{\beta\pi}\left[\left(C\left(\sqrt{\beta\pi T_p} - \sqrt{\frac{T_p\pi}{\beta T^2}}k\right) - C\left(-\sqrt{\frac{T_p\pi}{\beta T^2}}k\right)\right)^2 \right. \\ \qquad \left. + \left(S\left(\sqrt{\beta\pi T_p} - \sqrt{\frac{T_p\pi}{\beta T^2}}k\right) - S\left(-\sqrt{\frac{T_p\pi}{\beta T^2}}k\right)\right)^2\right] & k \le 0 \\ \frac{1}{T^2}\frac{T_p}{\beta\pi}\left[\left(C\left(\sqrt{\frac{T_p\pi}{\beta T^2}}k\right) + C\left(\sqrt{\beta\pi T_p} - \sqrt{\frac{T_p\pi}{\beta T^2}}k\right)\right)^2 \right. \\ \qquad \left. + \left(S\left(\sqrt{\frac{T_p\pi}{\beta T^2}}k\right) + S\left(\sqrt{\beta\pi T_p} - \sqrt{\frac{T_p\pi}{\beta T^2}}k\right)\right)^2\right] & 0 \le k < T\beta \\ \frac{1}{T^2}\frac{T_p}{\beta\pi}\left[\left(C\left(\sqrt{\frac{T_p\pi}{\beta T^2}}k\right) - C\left(-\sqrt{\beta\pi T_p} + \sqrt{\frac{T_p\pi}{\beta T^2}}k\right)\right)^2 \right. \\ \qquad \left. + \left(S\left(\sqrt{\frac{T_p\pi}{\beta T^2}}k\right) - S\left(-\sqrt{\beta\pi T_p} + \sqrt{\frac{T_p\pi}{\beta T^2}}k\right)\right)^2\right] & T\beta \le k, \end{cases}$$

where the Fresnel integrals [12, p. 615] are defined as

$$C(z) \triangleq \sqrt{\frac{2}{\pi}}\int_0^z \cos(x^2)dx \quad \text{and} \quad S(z) \triangleq \sqrt{\frac{2}{\pi}}\int_0^z \sin(x^2)dx.$$

The spectrum is composed of spectral lines spaced at harmonics of the waveform repetition rate. The main lobe bandwidth of the waveform is approximately β Hz. Figure 19(a) contains a plot of the power of the signal in 1-Hz increments for a waveform with β = 40 MHz, T = 12 ms, and a 100 percent duty cycle where the origin has been shifted from $\beta/2$ to 0. The βT_p product of this signal is very large at 480000, resulting in a nearly ideal rectangular spectrum. Reducing the duty cycle to 10 percent reduces the βT_p product; however, at such a large value, little change in the rectangular spectrum is evident, as shown in Figure 19(b). The reduction in the duty cycle does, however, reduce the power by 10 dB. Reducing the waveform duration to T = 8 μs with a 50 percent duty cycle reduces the βT_p product to 160, with a noticeable degradation in the rectangular shape of the spectrum, as shown in Figure 20. The shorter duration also increases the line spacing, resulting in sparser spectral lines of higher power.

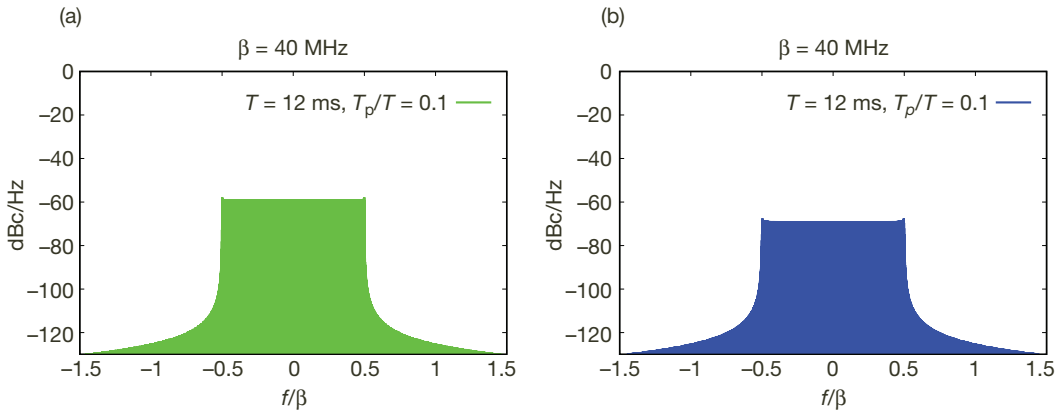

Figure 19. The spectral power in 1-Hz intervals for a pair of LFM waveforms with equal bandwidths, β = 40 MHz, and periods T = 12 ms: (a) T_p/T = 1; (b) T_p/T = 01.

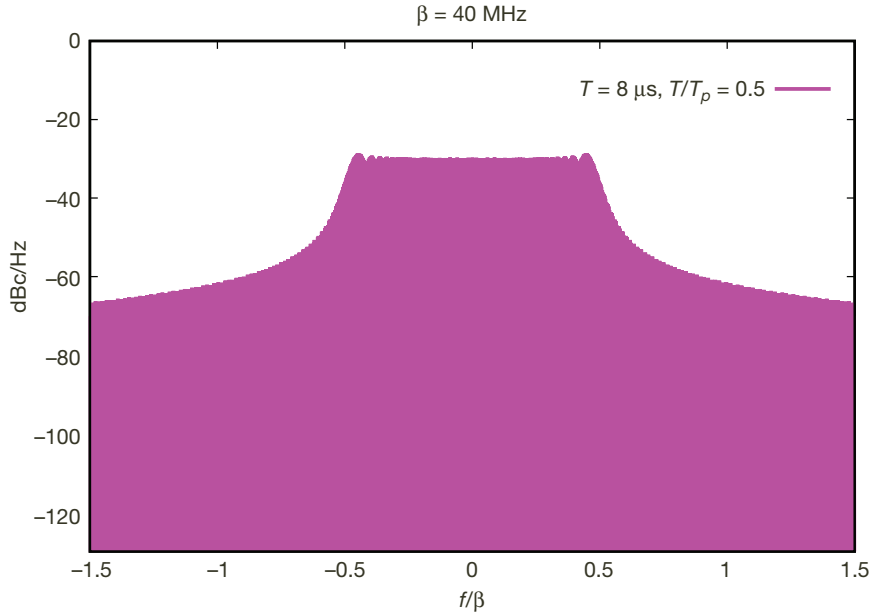

Figure 20. The power spectrum of the LFM waveform evaluated in 1-Hz intervals.

D. Ambiguity Function

The ambiguity function of a signal with period T is defined as

$$\xi(\tau,\omega_d) \triangleq \frac{1}{T}\int_{-T/2}^{T/2} z(t)z(t+\tau)e^{j\omega_d t}dt \quad -T/2 \le \tau < T/2.$$

Evaluating this, we have

$$\begin{aligned}\xi(\tau,f_d) &= \frac{1}{T}\int_{-T/2}^{T/2} z(t)z(t+\tau)dt \quad -T/2 \le \tau < T/2 \\ &= \frac{1}{2}\Re\left\{\tilde{\xi}(\tau,f_d)e^{j\omega_c\tau}\right\} \quad |\tau| \le T/2, \end{aligned} \tag{15}$$

where

$$\begin{aligned}\tilde{\xi}(\tau,f_d) = \gamma(\tau+T,f_d)\big(u(\tau+T)-u(\tau+(T-T_p))\big)+\gamma(\tau,f_d)\big(u(\tau+T_p)-u(\tau-T_p)\big) \\ +\gamma(\tau-T,f_d)\big(u(\tau-(T-T_p))-u(\tau-T)\big) \quad |\tau| \le T/2,\end{aligned}$$

with

$$\gamma(\tau,f_d) \triangleq e^{-j\pi[(f_d+\beta)\tau+f_dT_p]}\frac{(T_p-|\tau|)}{T}\frac{\sin\left(\pi\left(f_d-\frac{\beta}{T_p}\tau\right)(T_p-|\tau|)\right)}{\pi\left(f_d-\frac{\beta}{T_p}\tau\right))(T_p-|\tau|)}.$$

Examining Equation (15), we note, as with the autocorrelation, that the ambiguity function is dominated by a $sin(x)/x$-type response with respect to the delay. The peak value of the $sin(x)/x$ term occurs at

$$\tau_{peak} = \frac{f_dT_p}{\beta}.$$

A return with a Doppler offset will elicit nearly the same response, sans the $1-|\tau|$ scaling, as a return at delay $\tau = \frac{f_dT_p}{\beta}$. This Doppler delay coupling is the salient feature (or bane depending on your perspective) of LFM and will appear as ridge running through the origin of the delay Doppler plane with an attenuation of $1-|\tau|$ away from the origin. Taking into consideration that the period of the waveform is T, unambiguous Doppler measurements can be made between $-1/2T$ and $1/2T$, giving an effective Doppler bandwidth, due to the delay Doppler coupling, of

$$B_{D_{eff}} = \frac{1}{T}.$$

Assuming the Doppler extent of the object is on this order, we note that a Doppler offset of $f_d = 1/(2T)$ will result in a delay coupling of

$$\hat{\tau} = \frac{T_p}{T}\frac{1}{2\beta}.$$

This falls within the delay resolution of the waveform and can be reduced, at the cost of returned energy, by reducing the duty cycle of the waveform. Turning to the sidelobe structure, for $\beta T_p >> 1$, the sidelobes moving away from the ridge have sidelobe nulls occurring at

$$\frac{f_d T_p \beta - n}{f_d + \beta} \quad n = \pm 1, \pm 2, \cdots$$

and peaks occurring at

$$\frac{f_d T_p \beta - \frac{2n+1}{2}}{f_d + \beta} \quad n = \pm 1, \pm 2, \cdots.$$

The first sidelobe will have a level at –13.4 dB with respect to the corresponding ridge, and the subsequent sidelobes will decay with the inverse distance to the ridge. The phase of the ambiguity function,

$$\pi\left[(\omega_c + \beta + f_d)\tau + f_d T_p\right],$$

varies linearly with respect to τ with a slop of $\omega_c + \beta + f_d$.

The magnitude square of the ambiguity function of the complex baseband signal is plotted in Figure 21 for an LFM waveform with a 100 percent duty cycle, $T_p = T$, and a βT_p product of 48000. The domain encompassing the main lobe is shown in order to demonstrate the ridge and sidelobe structure of the function. The delay Doppler coupling that provides an effective Doppler bandwidth equal to the unambiguous Doppler bandwidth is evident. The first sidelobe from the ridge has a level of –13.4 dB, and subsequent sidelobes decay from the ridge as a sinc function.

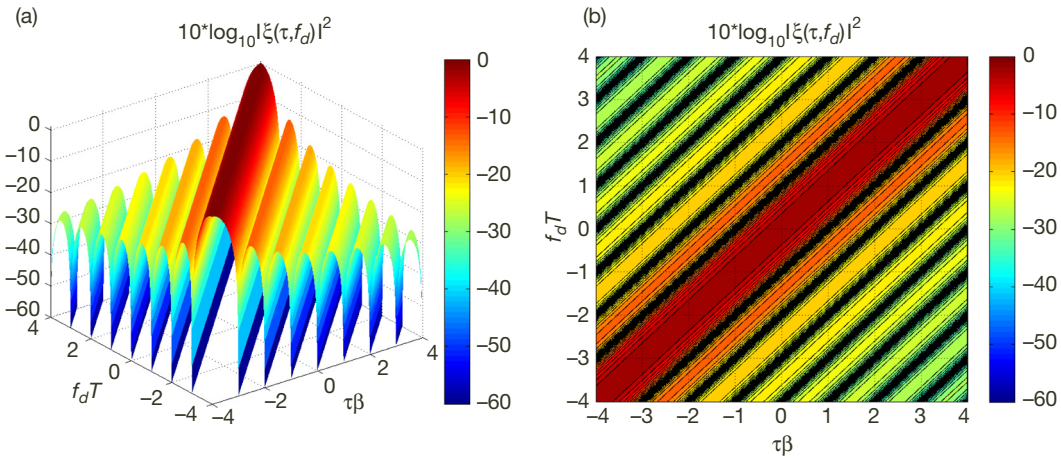

Figure 21. Ambiguity function of LFM waveform with β = 40 MHz, T_p = 12 ms, T = 12 ms: (a) 3-d plot; (b) contour plot.

E. Windowing

As with Costas-FH in Section V.E, the relatively high sidelobe levels of the LFM ambiguity function, starting at –13.4 dB, can be reduced through the use of windowing functions. Several options are available, including Taylor and Hamming window functions, which will reduce the peak sidelobe to less than –40 dB at the cost of less than 1.5 dB in SNR and increase in the main lobe width, degrading the resolution, by at most 150 percent [11, p. 345][3, pp. 612–618]. To verify this, we consider the effect of a Hamming window on the autocorrelation function.

The complex baseband autocorrelation, Equation (14), in the region $|\tau| \leq T_p$, and assuming $\beta T >> 1$, can be approximated as

$$\tilde{r}(\tau) \approx e^{-j\pi\beta\tau}\frac{T_p}{T}\frac{\sin(\pi\beta\tau)}{\pi\beta\tau}.$$

Applying a Hamming window $H(\omega)$, Equation (11), to the received signal in the frequency domain will result in an autocorrelation, $\tilde{r}_w(\tau)$, of

$$\begin{aligned}
\tilde{r}_w(\tau) &= \mathcal{F}^{-1}\left\{\mathcal{F}\left(f-\frac{\beta}{2}\right)\right\} \\
&= \mathcal{F}^{-1}\left\{\frac{T_p}{T}\mathrm{rect}\left(\frac{f}{\beta}-\frac{1}{2}\right)H\left(f-\frac{\beta}{2}\right)\right\} \\
&= \frac{T_p}{T}e^{-j\pi\beta\tau}\int_{-\frac{\beta}{2}}^{\frac{\beta}{2}}\left(0.08+0.92\cos^2\left(\pi\frac{f}{\beta}\right)\right)e^{j2\pi ft}df \\
&= e^{-j\pi\beta\tau}\left(0.08+\frac{0.46}{1-(\tau\beta)^2}\right)\frac{\sin(\pi\beta\tau)}{\pi\beta\tau}. \qquad (16)
\end{aligned}$$

In Figure 22, the complex baseband autocorrelation, Equation (14), along with the autocorrelation of the windowed system, Equation (16), is shown. The windowed system has sidelobes at –43.5 dB with respect to the peak. The 3 dB and 6 dB extents of the main lobe are approximately 1.5 times wider than that of the unwindowed system; the corresponding delay resolutions are therefore

$$\Delta_{3\,dB} = \frac{1.3}{\beta}$$
$$\Delta_{6\,dB} = \frac{1.8}{\beta}.$$

The loss in SNR for this Hamming window was given in Equation (13) at –1.34 dB.

F. Waveform Characteristics Summary

For the LFM waveform with a main lobe bandwidth B, a period T, and a full duty cycle, $T_p = T$, the waveform characteristics are summarized in terms of these parameters (Table 4):

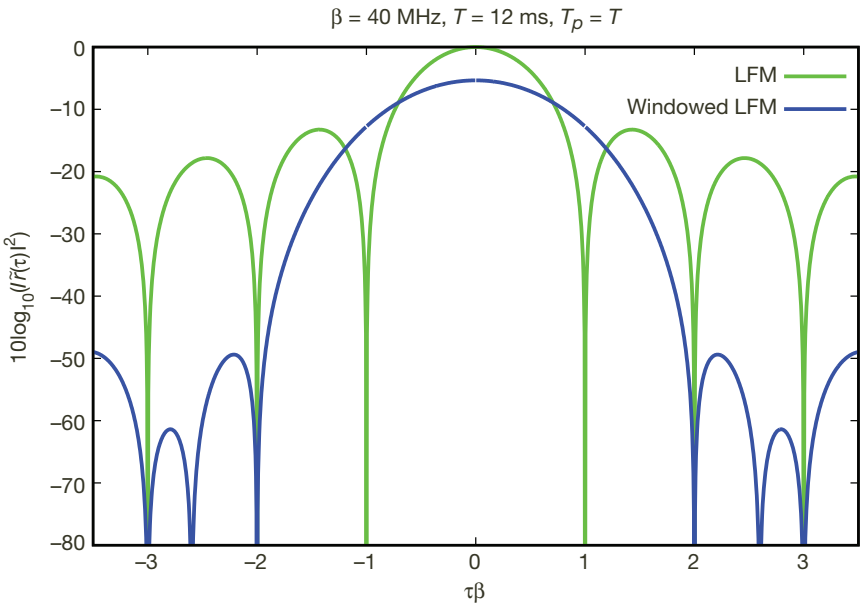

Figure 22. LFM autocorrelation function with and without Hamming window, $\beta = 40$ MHz, $T = T_p = 12$ ms.

Table 4. Summary of LFM waveform characteristics.

	LFM	Windowed LFM
Unambiguous Delay Depth	T	T
Delay Resolution	$\Delta_{3\,dB} = \frac{0.88}{B}$ $\Delta_{6\,dB} = \frac{1.2}{B}$	$\Delta_{3\,dB} = \frac{1.3}{B}$ $\Delta_{6\,dB} = \frac{1.8}{B}$
Unambiguous Doppler Bandwidth	$\frac{1}{T}$	$\frac{1}{T}$
Effective Doppler Bandwidth	$B_{D_{eff}} = \frac{1}{T}$	$B_{D_{eff}} = \frac{1}{T}$
Peak Ambiguity Sidelobe	$\xi_{peak} = -13.4$ dB	$\xi_{peak} = -43.5$ dB

VII. Requirements

Candidate waveforms for the GSSR observation of the lunar surface must meet certain criteria dictated by the observation as well as constraints imposed by the transmission and reception of the modulation. The most significant of these criteria and constraints form a set of requirements for the waveform and are grouped into three areas: lunar observation, spectrum allocation, and klystron power amplifier.

A. Lunar Observation

For a radar observation at a given wavelength, the parameters most pertinent to the selection of a modulation are the delay depth, Doppler bandwidth, and the dynamic range of

the radar cross-section of the object to be observed. The delay depth and Doppler bandwidth can be used to set the period of the waveform, which, along with the bandwidth of the waveform, will dictate the peak ambiguity function sidelobe level of that waveform. This peak sidelobe level must be sufficient to suppress the entire dynamic range of the radar cross-section in order to mitigate bright objects from obscuring the detection of other features. The expected delay depth, Doppler bandwidth, and radar cross-section dynamic range for an observation in the lunar polar region are given. Table 5 contains the lunar observation parameters assumed in these calculations.

Table 5. Lunar observation parameters.

Distance to the Moon	D = 380,000 km
Radius of the Moon	R_m = 1,737 km
Rotation Rate of the Moon	ω_m = 2.66 μrad/s
Orbital Period of the Moon	T_m = 27.32 days
Radius of Earth	R_e = 6,378 km
Rotation Rate of Earth	ω_e = 73 μrad/s
Latitude of the GSSR	ϕ = 0.61 rad
Transmission Wavelength	λ = 0.035 m
Beamwidth of the 70-m Antenna	ψ = 1.2 mrad

As the rotational period of the Moon is equal to its orbital period, we can set a rotating frame of reference for an observer at the center of Earth with the Moon appearing stationary. For simplicity, the Moon is assumed to orbit along the celestial equator. A radar on the surface of Earth observing a point on the surface of the Moon will only see a Doppler contribution due to the rotation of Earth in this frame. To find the Doppler frequency offset, consider the geometry shown in Figure 23. Using this figure, we find the Doppler frequency shift is given by

$$F_d = \frac{2R_e \cos(\phi)\omega \cos(\alpha)}{\lambda}, \tag{17}$$

where ϕ is the latitude of the radar, α is the angle from the western horizon to the Moon, and the rotation rate of Earth in this frame is

$$\omega = \omega_e - \frac{2\pi}{T_m}.$$

The limb-to-limb Doppler bandwidth is the change in Doppler frequency between observation points on opposite edges of the Moon, as shown in Figure 24. Using this figure, the change in Doppler is

$$\begin{aligned} B_m &\triangleq \frac{2R_e \cos(\phi)\omega}{\lambda}\left[\cos(\alpha_0) - \cos(\alpha_1)\right] \\ &= \frac{2R_e \cos(\phi)\omega}{\lambda} 2\sin\left(\frac{\alpha_1 - \alpha_0}{2}\right)\sin\left(\frac{\alpha_1 + \alpha_0}{2}\right), \end{aligned}$$

where α_0 and α_1 are the observation angles from the western horizon. Using the approximations

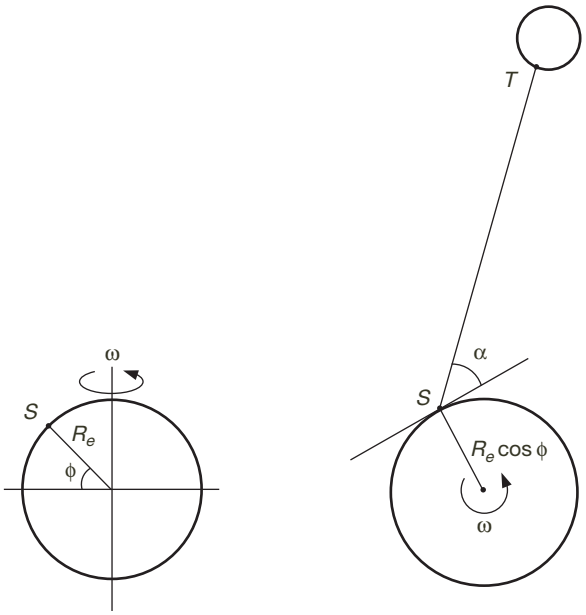

Figure 23. Radar at point *S* on the surface of Earth at latitude angle ϕ observing point *T* on the lunar surface, with the Moon at elevation angle α with respect to the observer. Side and top views shown.

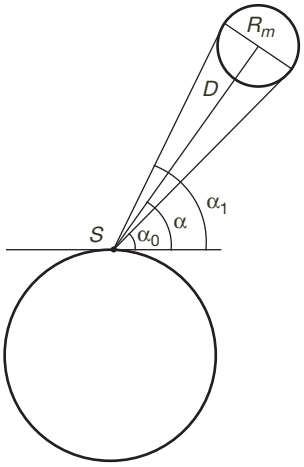

Figure 24. Diagram showing angular difference between limb-to-limb observation points on the Moon.

$$\alpha_0 \approx \alpha - \gamma \quad \text{and} \quad \alpha_1 \approx \alpha + \gamma$$

along with

$$\sin(\gamma) = \frac{R_m}{D}$$

we have a limb-to-limb Doppler bandwidth of

$$B_m = \frac{4R_e \cos(\phi)\omega R_m \sin(\alpha)}{D\lambda}.$$

Bounding this by setting $\alpha = \pi/2$ gives

$$B_m < 192 \text{ Hz}.$$

From Figure 24, we also note that the Moon has a delay depth of

$$\tau_m \triangleq \frac{2R_m}{c} = 11.6 \text{ ms}.$$

While returns from the full lunar extent can be evident, those in the region illuminated by the main beam of the antenna will dominate. Assuming radar illumination using a 70-m antenna, a first-order measure of the delay depth and Doppler bandwidth of the region illuminated by the 3-dB beamwidth of the antenna for an observation near the limb is obtained by considering the geometry shown in Figure 25. The delay depth of the illuminated region is calculated from the length of the illuminated region in the line of sight,

$$\tau_i \triangleq \frac{2\sqrt{R_m^2 - \left(R_m - 2D\sin\left(\frac{\Psi}{2}\right)\right)^2}}{c} = 7.8 \text{ ms},$$

where ψ is the main lobe beamwidth of the 70-m antenna at DSS-14. The Doppler bandwidth of the illuminated region is found by scaling the Doppler bandwidth of the Moon by the ratio of the cross-line of sight illumination length to the lunar diameter [13], giving

$$B_i \triangleq \frac{2D\sin\left(\frac{\Psi}{2}\right)}{2R_m} B_m = 25 \text{ Hz}.$$

The distortion of the waveform time-base between transmission and reception of echoes, due to the known motion between the transmitting and receiving stations on Earth and the target on the lunar surface, can be compensated for either during transmission or reception. Typically this is done by predistorting the transmitted signal during transmission in order to both keep the received signal centered in the passband of the receiver front-end and to reduce the computational requirements and fidelity of the received data. From Equation (17), to a first order, the magnitude of the Doppler frequency offset will be F_d = 21 kHz; for Doppler offsets in the kHz range, the passband of the receiver is not a concern.

Aliasing in delay will occur if the period of the waveform does not exceed the delay spread of the object. Assuming the distortion of the time-base has been compensated for, to avoid

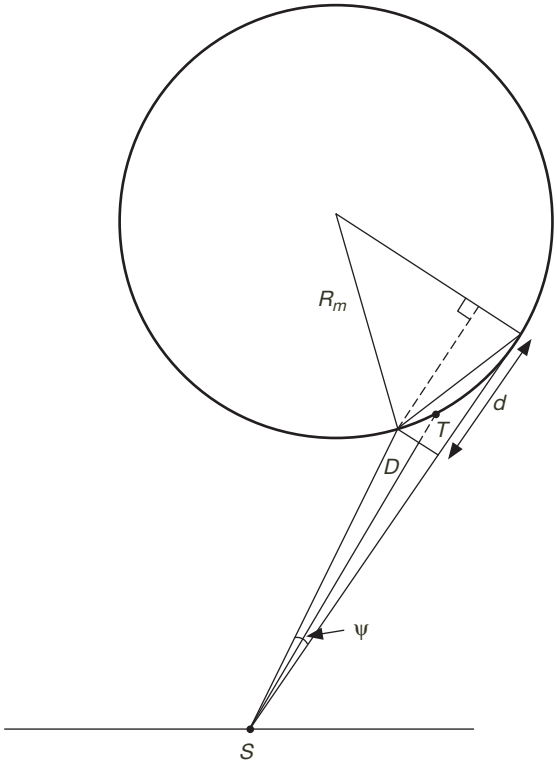

Figure 25. Diagram showing illuminated area and delay depth at the limb of the Moon.

aliasing in the Doppler domain, the repetition rate of the waveform must exceed the Doppler bandwidth. This ensures that, for uniform sampling, the Nyquist sampling rate criteria of twice the highest Doppler frequency offset is met. Using the delay spread of the Moon along with the Doppler bandwidth of the illuminated region, to avoid both range and Doppler aliasing the period of the waveform, T, should fall with

$$11.6 \text{ ms} < T \leq 40 \text{ ms}.$$

For a given waveform, the domain over which it can effectively measure Doppler shifts is $[-\frac{B_{eff}}{2}, \frac{B_{eff}}{2}]$, where B_{eff} is defined as the 1 dB extent of the ambiguity function in the Doppler axis at a delay of zero, $\tau = 0$. To effectively measure the Doppler offset of a return, the effective Doppler bandwidth of the waveform should be encompass the Doppler bandwidth of the illuminated area

$$B_{eff} \geq B_i = 25 \text{ Hz}.$$

From Equation (14), the radar cross-section of the lunar surface at a wavelength of 3.8 cm ranges from –0.8 dB to –30 dB for incident angles from 2 deg to 85 deg. The peak ambiguity function sidelobe level, ξ_{peak}, must be sufficient to cover this dynamic range:

$$\xi_{peak} < -30 \text{ dB}.$$

B. Spectrum Allocation

The GSSR spectrum allocation is to transmit a maximum of 600 kW between 8500 MHz and 8620 MHz.[1] To meet both DSN protection criteria [15] and near-Earth protection criteria [16], out-of-band power must be limited to less than –221 dB W/Hz between 8400 to 8450 MHz and less than –216 dB W/Hz between 8450 to 8500 MHz, respectively. To determine a requirement on the out-of-band power level for the candidate modulations, both the transmitted and returned signals must meet the protection criteria.

We first consider the out-of-band received power due to the return signal. In this case, the out-of-band received power P_r may be calculated from the radar equation [17, pp. 672–675] as

$$P_r = P_t \frac{G_t G_r \lambda^2}{64\pi^3 D^4} \sigma S_m, \tag{18}$$

where P_t is the transmitted power, G_t is the transmitter antenna gain, G_r is the receiver antenna gain, D is the distance to the Moon, σ is the radar cross-section, and S_m is a factor representing the spectral level of the modulation at the desired frequency. The values we use for this calculation are:

P_t	465 kW [18]
λ	0.035 m
G_t	74.5 dB (70-m)
G_r	68 dB (34-m)
D	3.8×10^8 m
σ	–0.8 dB (2-deg incident angle) to –30 dB (85-deg incident angle) [14]

Using the largest radar cross-section value, we solve Equation (18) for S_m. To meet the protection criteria on the returned signal, the maximum out-of-band power should be

$$S_m < -9.1 \text{ dBc/Hz}.$$

For the out-of-band received power due to the transmitted signal, we note that the GSSR currently supports and regularly transmits from DSS-14 both CW and BPC radar waveforms as well as an LFM waveform on a developmental basis. The spectrum of a GSSR waveform consists of discrete spectral lines spaced at harmonics of the repetition rate. Using the regularly transmitted 0.125-μs BPC waveform with a period of 16.4 ms, the spectral lines are spaced at 61-Hz increments. In Figures 26(a) and (b), theoretical curves of the power in 1-Hz increments are shown over the entire GSSR spectrum allocation and adjacent bands and at the edge of the GSSR spectrum allocation, respectively. The 61-Hz line spacing and peak out-of-band sidelobe level of –78 dBc/Hz are noted.

To calculate the out-of-band-power due to the transmitted signal, we consider the direct reception of this signal at the other stations. For DSS-15, at only 0.5 km away, schedule coordination is used to avoid GSSR transmission by DSS-14 while DSS-15 is in use. For the other

[1] NASA97312, Government Master File Database, National Telecommunications and Information Administration.

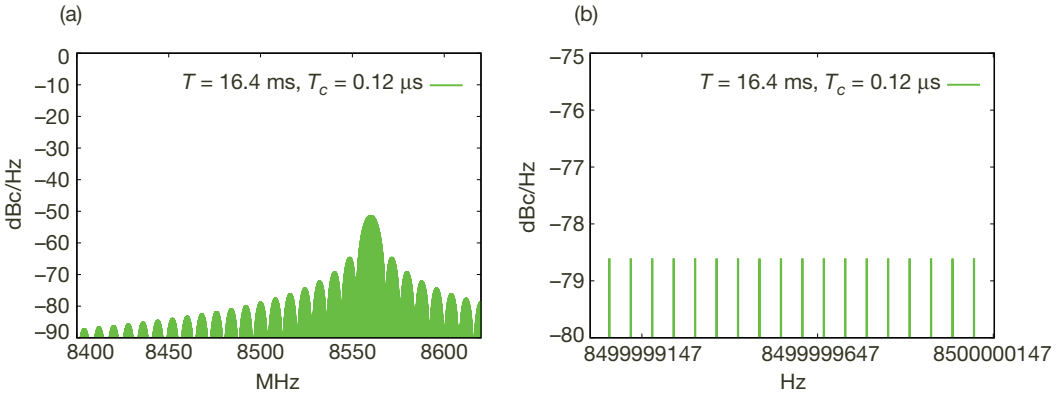

Figure 26. The spectral power in 1-Hz intervals for a BPC waveforms with T_c = 0.125 µs and a code period $M = 2^{17}–1$: (a) entire GSSR spectrum allocation and adjacent bands; (b) band-edge of the GSSR allocation.

stations, we bound the path loss to the second nearest station with the free-space path loss and use the Friis power transmission formula [19, pp. 48–49]

$$P_r = P_t \frac{G_t G_r \lambda^2}{16\pi^2 D^2} S_m. \tag{19}$$

At 8500 MHz, the sidelobe level of the BPC waveform is S_m = –78 dBc/Hz. Assuming a transmit power of P_t = 465 kW and using the path loss to the second nearest station, DSS-16, located D = 9.5 km away, for Equation (19), a near-field coupled antenna gain, $G_t G_r$, exceeding –64 dB would violate the –216 dB W/Hz protection criteria. No near-field antenna gain patterns for DSS-14 and adjacent stations have been made. A study investigating radio frequency interference (RFI) from the GSSR at DSS-12 and DSS-16 concluded that the GSSR did not exceed spectrum limitations at S-band and because of diffraction effects the X-band RFI was expected to be lower.[2] The BPC waveform spectrum outside the allocated band will therefore be used as a spectral mask for the candidate modulations with regard to the received out-of-band power due to the transmitted signal; the modulation used for the lunar observations will have out-of-band power levels less than those of the 0.125 μs BPC 16.38 ms waveform, which has a maximum out-of-band spectral component of –78 dBc.

The –78 dBc/Hz constraint on received out-of-band power due to the transmitted signal exceeds the –9.1 dBc/Hz constraint due to the received out-of-band power from the returned signal and will be used as a selection criteria for the candidate waveforms. During the development process, before transmission of a new waveform, measurements will be conducted as necessary to validate that all protection criteria are met.

C. Klystron Power Amplifier

To achieve the 400-kW-rated transmit power of the GSSR, the outputs from a pair of 250-kW klystron power amplifiers are combined to form the RF modulated signal that is transmitted, with a 20 percent loss, through the 70-m antenna at DSS-14. Each klystron

[2] T. Peng, "Radar RFI at Goldstone DSS-12 and DSS-16, Final Report," JPL Interoffice Memorandum 3393-89-126 (internal document), Jet Propulsion Laboratory, Pasadena, California, November 1989.

can operate in saturation between 8547.5 MHz and 8582.5 MHz [20][3]; this frequency range represents the 1-dB bandwidth of the amplifier. The phase linearity of the amplifier is specified in two ranges; for frequencies within 8560 MHz ±9 MHz, the phase is linear to within ±3 deg, for frequencies within 8560 MHz ±30 MHz, the phase is linear to within ±15 deg [20].[4] To avoid damaging levels of body current [21], for modulations with a discontinuous phase, the phase switch rate of signals is limited to 8 MHz, and, for all signals, significant spectral content outside the passband should be limited.

The bandwidth of the klystron limits the transmit signal to have a main lobe spectral bandwidth of less than 45 MHz. As the transmitted signal is commonly precompensated for Doppler frequency offsets of up to ±4.1 MHz, the main lobe spectral bandwidth for the GSSR is restricted to 40 MHz; as noted, for lunar observations the maximum Doppler frequency offset will be on the order of 21 kHz; we, however, maintain the 40 MHz main lobe spectral bandwidth limitation in order to be compatible with the bulk of nonlunar observations. The phase linearity over the entire band can be off by as much as ±15 deg for a single klystron. At the band edge of 8580 MHz, this could result in an additional 0.15 dB loss when combining the klystron output pair. The phase nonlinearity of the pair will distort the transmitted waveform; however, this distortion is constant over time and temperature and can thus be calibrated for at the receiver.

D. Requirements Summary

Candidate modulations for the GSSR observations of the Moon must have the following characteristics (Table 6) in order to meet the observational, spectrum allocation, and klystron power amplifier requirements:

Table 6. Summary of GSSR waveform requirements.

Repetition Period	$11.6 \text{ ms} < T \leq 40 \text{ ms}$
Effective Doppler Bandwidth	$B_{D_{eff}} = 25 \text{ Hz}$
Peak Ambiguity Sidelobe	$\xi_{\max} < -30 \text{ dB}$
Main Lobe Spectral Bandwidth	$B \leq 40 \text{ MHz}$
Peak Out-of-Band Spectral Sidelobe	$S_{\max} \leq -78 \text{ dBc/Hz}$
Maximum Phase Switch Rate	8 MHz

VIII. Comparison

To select among the candidate waveforms, from Section VII we have a set of criteria, shown in Table 6, that are necessary in order to meet the observational, spectrum allocation, and klystron power amplifier requirements.

[3] "Klystron Amplifier 250-kW X-Band Transmitter DSCC Transmitter Subsystem," JPL Detail Specification ES513821, Rev. E (internal document), Jet Propulsion Laboratory, Pasadena, California, February 2000.

[4] Ibid.

Using these to set the period, T, and bandwidth, B, of the candidate waveforms, the waveform characteristics, given in terms of B and T in Sections III.E, IV.E, V.F, and VI.F can be solved to give the resulting waveform characteristics for GSSR lunar observations shown in Table 7.

Table 7. Characteristics of GSSR candidate waveforms for lunar observations.

Waveform	Bandwidth	Period	Resolution		Effective Doppler Bandwidth	Peak Ambiguity Sidelobe	Peak Out-of-Band Spectral Sidelobe
			$\Delta_{6\,dB}$	$\Delta_{3\,dB}$			
BPC	16 MHz	16.4 ms	18.75 m	11 m	30.4 Hz	–51 dB	–78 dBc/Hz
MSK	40 MHz	19.7 ms	9 m	6.3 m	25.4 Hz	–54 dB	–95 dBc/Hz
Costas-FH	40 MHz	11.9 ms	4.5 m	3.3 m	42 Hz	–13.4 dB	–123 dBc/Hz
Windowed Costas-FH	40 MHz	11.9 ms	6.75 m	5 m	—	–43.5 dB	–123 dBc/Hz
LFM	40 MHz	12 ms	4.5 m	3.3 m	83 Hz	–13.4 dB	–129 dBc/Hz
Windowed LFM	40 MHz	12 ms	6.75 m	5 m	83 Hz	–43.5 dB	–129 dBc/Hz

From Table 7, BPC, MSK, FH-windowed, and LFM-windowed meet the spectrum, klystron power amplifier, and science constraints of a GSSR lunar observation. Neither LFM nor Costas-FH meet the –30 dB peak ambiguity function sidelobe necessary to handle the 30-dB dynamic range of the lunar backscatter; however, by applying spectral windowing to the received signal, the ambiguity function sidelobes of LFM and Costas FH can be reduced to meet the peak ambiguity sidelobe requirement at the expense of SNR and resolution, as shown in the characteristics of windowed Costas-FH and windowed LFM waveforms.

The $\Delta_{3\,dB}$ and $\Delta_{6\,dB}$ range resolutions, converted from delay resolutions using

$$\Delta_r = \frac{\Delta_\tau c}{2}$$

are given for each of the waveforms. Two resolution metrics are provided, as both appear in the literature and their efficacy is presumed to be application dependent. The $\Delta_{3\,dB}$ resolution is the half-power extent of the main lobe of the waveform autocorrelation [1, pp. 88–93] and corresponds to the delay extent presented by a single echo. The $\Delta_{6\,dB}$ resolution is the half-magnitude extent of the main lobe of the waveform autocorrelation. This corresponds to a definition of resolution as the minimum delay between two equal power echoes that results in identifiable peaks in the matched filter output [1, pp. 88–89] [22, pp. 166–167].

The BPC waveform has a discontinuous phase and is limited to the 8-MHz maximum phase switch rate of the klystron power amplifier. The other waveforms have a continuous phase and are thus not subject to the phase switch rate limitation of the klystron. The klystron does, however, have a nonlinear phase response that will affect all the waveforms. From Section VII.C, the phase linearity specification of a single klystron is ±9 deg, 8560 MHz ±30 MHz; and ±3 deg, 8560 MHz ±9 MHz.

The LFM, FH, and MSK waveforms, which have approximately 55 percent, 55 percent, and 58 percent, respectively, of their spectral content outside the ±3 deg range, will be affected to a greater degree than BPC, which has only 10 percent of its spectral content outside this range. As the phase response of a klystron pair is stable over time and temperature, measurements of the response can be taken and compensated for in the receive signal processing, thus mitigating the degradation in SNR and resolution due to the phase nonlinearity.

IX. Conclusion

To identify radar waveforms for development consideration as GSSR ranging waveforms for lunar observations, several candidate waveforms were identified and analytically characterized. These included the existing GSSR BPC waveform; two well-known waveforms, LFM and Costas-FH; and an MSK-type waveform developed during the course of this study. A set of requirements taking into consideration the spectrum allocation of the GSSR, the limitations of the transmit power amplifier, and the science objectives for a lunar observation were developed and used as selection criteria for the candidate waveforms. Windowed LFM, windowed Costas-FH, MSK, and BPC waveforms were found to meet the requirements. Windowed LFM, windowed Costas-FH and MSK, with windowed LFM and windowed Costas-FH having the best range resolution, are therefore candidates for development consideration as a new GSSR ranging waveform for lunar observations.

References

[1] August Rihaczek, *Principles of High-Resolution Radar*, 3rd edition, New York, New York: McGraw-Hill, 2001.

[2] Nadav Levanon and Eli Mozeson, *Radar Signals*, Hoboken, New Jersey: John Wiley, 2004.

[3] Fred E. Nathanson, J. Patrick Reilly, and Marvin N. Cohen, *Radar Design Principles*, 2nd edition, New York, New York: McGraw-Hill, 1991.

[4] Miroslav L. Dukic and Zoran S. Dobrosavljevic, "A Method of a Spread-Spectrum Radar Polyphase Code Design," *IEEE Journal on Selected Areas in Communications*, vol. 8, no. 5, pp. 743–749, June 1990.

[5] John P. Costas, "A Study of a Class of Detection Waveforms Having Nearly Ideal Range-Doppler Ambiguity Properties," *Proceedings of the IEEE*, vol. 72, no. 8, pp. 996–1009, August 1984.

[6] Chieh-Fu Chang and Mark R. Bell, "Frequency-Coded Waveforms for Enhanced Delay-Doppler Resolution," *IEEE Transactions on Information Theory*, vol. 49, no. 11, pp. 2960–2971, November 2003.

[7] K. J. Quirk and M. Srinivasan, "An MSK Waveform for Radar Applications," *2009 IEEE Global Telecommunications Conference (GLOBECOM)*, Honolulu, Hawaii, pp. 1–6, November 2009.

[8] Dilip V. Sarwate and Michael B. Pursley, "Crosscorrelation Properties of Pseudorandom and Related Sequences," *Proceedings of the IEEE*, vol. 68, no. 5, pp. 593–619, May 1980.

[9] Steve C. Cripps, *RF Power Amplifiers for Wireless Communications*, Noorwood, Massachusetts: Artech House, 1999.

[10] Fred J. Harris, "On the Use of Windows for Harmonic Analysis with the Discrete Fourier Transform," *Proceedings of the IEEE*, vol. 66, no. 1, pp. 51–83, January 1978.

[11] Merrill I. Skolnik, *Introduction to Radar Systems*, New York, New York: McGraw-Hill, 1969.

[12] F. B. Hildebrand, *Advanced Calculus for Applications*, Englewood Cliffs, New Jersey: Prentice-Hall, 2nd edition, 1976.

[13] Jean-Luc Margot, Donald B. Campbell, Raymond F. Jurgens, and Martin A. Slade, "Digital Elevation Models of the Moon from Earth-Based Radar Interferometry," *IEEE Transactions on Geoscience and Remote Sensing*, vol. 38, no. 2, pp. 1122–1133, March 2000.

[14] T. Hagfors, "Remote Probing of the Moon by Infrared and Microwave Emissions and By Radar," *Radio Science*, vol. 5, no. 2, pp. 189–227, February 1970.

[15] "Protection Criteria for Deep-Space Research," Recommendation ITU-R SA 1157-1, International Telecommunication Union: http://www.itu.int/

[16] "Protection Criteria for Radiocommunication Links for Manned and Unmanned Near-Earth Research Satellites," Recommendation ITU-R SA 609-2," International Telecommunication Union: http://www.itu.int/

[17] David M. Pozar, *Microwave Engineering*, 2nd edition, New York, New York: John Wiley & Sons, 1998.

[18] J. D. Dvorsky, N. A. Renzetti, and D. E. Fulton, "The Goldstone Solar System Radar: A Science Instrument for Planetary Research," JPL Publication 92-29 NASA-CR-192793, Jet Propulsion Laboratory, Pasadena, California, December 1992.

[19] John D. Kraus, *Antennas*, McGraw-Hill, New York, NY, 2nd edition, 1988.

[20] Klystron Amplifier Type VKX-7864B, Serial Number 108R1, test performance sheet, Communications & Power Industries, 2001.

[21] Reginald A. Cormier and Albert Mizuhara, "250-kW CW Klystron Amplifier for Planetary Radar," *IEEE Transactions on Microwave Theory and Techniques*, vol. 40, no. 6, pp. 1056–1062, June 1992.

[22] Mark A. Richards, *Fundamentals of Radar Signal Processing*, New York, New York: McGraw-Hill, 2005.